04.82.01

CNEA-NT 14/82

REPUBLICA ARGENTINA
COMISION NACIONAL DE ENERGIA ATOMICA
Dependiente de la Presidencia de la Nación

A STUDY OF FRICTION AND AXIAL EFFECTS IN PELLET-CLAD MECHANICAL INTERACTION

S. Harriague and J.E. Mayer

Buenos Aires
1982

A STUDY OF FRICTION AND AXIAL EFFECTS IN PELLET-CLAD MECHANICAL INTERACTION.

by S. Harriague(*) and J.E. Meyer(**)

An analysis is made of the effect of friction forces at the pellet-cladding contact points on the behaviour of a fuel rod under a power-up ramp.

A thermoelastic description of the pellets is given; the stiffness matrix and initial displacements are obtained from a finite element calculation. The cladding is considered to behave as a thermoelastic thin shell.

A method is developed to assemble the stiffness of each pellet and corresponding cladding section on a fuel rod, resulting in an explicit description of the whole stack. The assumption of thermoelasticity allows for a very fast calculation, even when including hundreds of pellets under an arbitrary axial distribution of power.

Results showing the pattern of friction and axial forces, and relative and localized displacements along the rod, are presented. In most cases, pellets at the top of the stack slide with respect to the clad. As a result of the build-up of axial forces due to friction, pellets at lower positions

in the fuel column may show, at the contact positions, no relative displacements with respect to the cladding.

The effect of pellet dishing and L/D ratio on the axial strains and local deformations are shown. The predictions are consistent with the experimental observations on the effect of pellet shape.

Finally, a discussion is made of the results of this study. The use of these results as a guideline for establishing proper boundary conditions in a non-linear PCMI model (i.e., including plasticity and pellet cracking) are also discussed.

(*) Dept. de Materiales, Comisión Nacional de Energía Atómica, Buenos Aires, Argentina.

(**) Dept. of Nuclear Engineering, Massachusetts Institute of Technology, Cambridge, Mass., U.S.A.

1. INTRODUCTION

During the last years, many models have been developed for the analysis of pellet clad mechanical interaction at pellet interfaces (1-12, 32). In those models a finite element study is performed; a single pellet is considered, and usually symmetry considerations restrict the analysis to half a pellet. On the other side, in some 1 and $1\frac{1}{2}$ dimensional fuel rod modeling codes (13, 14), axial coupling of rod sections is performed taking into account the overall effect of axial and friction forces along the rod.

The problems of thermal hourglassing and pellet-clad interaction have also been treated using analytical methods, restricted to a single pellet (15-19).

A considerable amount of experimental work has been done on pellet clad interaction; Bailey et al (20) have published a general review. The effect of pellet shape has been analysed. S. Aas (21), reviewing the Halden experience, shows that:

- Flat-ended pellets lead to larger clad elongation than dished ones.
- Increasing the L/D ratio of the pellet also leads to larger clad elongation.

- Dished pellets give higher ridges than flat-ended ones.
- Ridging increases with the L/D ratio of dished pellets. No such effect was found with flat-ended pellets.

Carter (22, 23) has published experimental results on the effects of pellet shape on strains in collapsible cladding during power-up ramps. Some of his conclusions, mainly on dished pellets, are:

- Circumferential ridges can be reduced by using pellets with small L/D; in particular, an abrupt increase in ridge height ocurred for $L/D > 0.5$.
- Rod axial strains seem to be reduced by decreasing L/D; if the rod is ramped to central melting, the opposite happens.
- Dished pellets with wider shoulders lead to smaller ridges and increasing axial strains.

Whatham (24) has measured ridges on pellet stacks electrically heated. He also finds an increase on ridging with the L/D ratio, and larger ridges for dished pellets than for flat-ended ones.

It is the purpose of this work to study the effect of friction and axial forces in a complete pellet stack interacting with the cladding. The analysis is therefore not restricted to a single pellet, and no symmetry considerations are involved to restrict the analysis to half a pellet.

In order to keep computer time within reasonable limits (stacks of up to 100 pellets will be modeled), a linear thermoelastic analysis is performed of both pellets and cladding. In order to take into account in some way effects of pellet cracking, pellet creep and plasticity, the ratio $\underline{e}$ of Young modulii of fuel and cladding is used as a parameter; qualitatively different behaviors of the rod are presented for different values of that ratio.

The behavior of the rod under a power-up ramp is studied. The reference state will be one where, for all pellets that will contact the cladding during the ramp, a zero gap, zero contact force situation exists. Fission gas release during the ramp, as well as changes in the fuel to clad heat conductance, are neglected.

In section 2 the method developed for the analysis of the rod is described. In section 3 a discussion is presented regarding the relative displacement of a single pellet and the cladding; stuck and sliding situations are analysed.

Section 4 presents the results regarding the behavior of fuel rods under different power distributions, as a function of pellet shape, friction coefficient and material parameters. Finally, the conclusions of this study are presented in section 5.

2. NUMERICAL METHOD

2.1 A method for the analysis of composite structures.

The method used in this work for the representation of a fuel rod is an extension of the one proposed by Fridrich (25) for composite structures.

Define a primitive form (P-form from now on) for a substructure by its stiffness matrix K_P and initial forces F_P° such that:

$$F_P = K_P . D_P + F_P^\circ \qquad (1)$$

where D_P is the displacement vector and F_P the force vector. In the present application, the substructure to which eq.(1) applies will be each pellet and its corresponding section of cladding.

Let a transformed representation (T-form) be defined by a matrix C_{PT} such that:

$$D_P = C_{PT} . D_T \qquad (2)$$

and

$$F_T = K_T . D_T + F_T^\circ \qquad (3)$$

The T-form corresponds essentially to a representation in the reference frame of the complete structure.

The equivalence of virtual work in the P and T forms leads to (see (25) for details):

$$F_T = C_{PT}^t \cdot F_P \quad (4)$$

$$K_T = C_{PT}^t \cdot K_P \cdot C_{PT} \quad (5)$$

$$F_T^o = C_{PT}^t \cdot F_P^o \quad (6)$$

where the superscript "t" means transpose.

The T-form may contain redundant degrees of freedom. In the case of a fuel rod, refundant degrees of freedom arise from imposing contact conditions of equal radial displacements for pellet and cladding, friction relationships between normal and tangential forces, axial equilibrium, etc.

Let n_T be the number of degrees of freedom in the T-form, and n_R the number of redundant degrees of freedom to be eliminated. The n_R redundancy conditions are generally expressed in matrix form as:

$$S_o + S_F \cdot F_T + S_D \cdot D_T = 0 \quad (7)$$

where S_O is n_R x 1; S_F and S_D are n_R x n_T.

The n_T degrees of freedom in the T representation are arranged in order to leave the n_R redundant ones at the bottom. The matrices in the T-form are written as:

$$F_T = \begin{array}{|c|}\hline F_I \\ \hline F_R \\ \hline\end{array} \begin{array}{l} \}\, n_T - n_R \\ \}\, n_R \end{array} \tag{8a}$$

$$D_T = \begin{array}{|c|}\hline D_W \\ \hline D_R \\ \hline\end{array} \tag{8b}$$

$$K_T = \begin{array}{|c|c|}\hline K_{II} & K_{IR} \\ \hline K_{RI} & K_{RR} \\ \hline\end{array} \tag{8c}$$

$$F_T^o = \begin{array}{|c|}\hline F_I^o \\ \hline F_R^o \\ \hline\end{array} \tag{8d}$$

where K_{II} is $(n_T - n_R) \times (n_T - n_R)$, K_{IR} is $(n_T - n_R) \times n_R$, K_{RI} is $n_R \times (n_T - n_R)$ and K_{RR} is $n_R \times n_R$. Due to the symmetry of the stiffness matrix, K_{II} and K_{RR} are symmetric and $K_{IR} = K_{RI}^t$.

The redundancy eqs. (7) are written as:

$$S_o + S_{FI} \cdot F_I + S_{FR} \cdot F_R + S_{DI} \cdot D_W + S_{DR} \cdot D_R = 0 \tag{9}$$

Eq. (3) can be expressed as:

$$F_I = K_{II} \cdot D_W + K_{IR} \cdot D_R + F_I^o \tag{10a}$$

$$F_R = K_{RI} \cdot D_W + K_{RR} \cdot D_R + F_R^o \tag{10b}$$

F_I and F_R are substituted in eq. (9). Calling:

$$M_o = S_o + S_{FI} \cdot F_I^o + S_{FR} \cdot F_R^o \qquad (11a)$$

$$M_R = S_{DR} + S_{FI} \cdot K_{IR} + S_{FR} \cdot K_{RR} \qquad (11b)$$

$$M_I = S_{DI} + S_{FI} \cdot K_{II} + S_{FR} \cdot K_{RI} \qquad (11c)$$

the redundant displacements D_R can be expressed as:

$$D_R = - M_R^{-1} M_I \, D_W - M_R^{-1} M_o$$

Let:

$$C_{TW} = M_R^{-1} M_I \qquad (12a)$$

$$D_R^* = - M_R^{-1} M_o \qquad (12b)$$

Then:

$$D_R = D_R^* - C_{TW} \cdot D_W$$

The $n_T - n_R = n_W$ degrees of freedom with the displacements D_W define the working-form (W-form). The demand of equal virtual work in the T-form and W-form allows the calculation of the conjugate forces F_W:

$$F_W^t \cdot \delta D_W = F_T^t \cdot \delta D_T \qquad (14)$$

As: $F_T^t \cdot \delta D_T = F_I^t \cdot \delta D_W + F_R^t \cdot \delta D_R$

using (13):

$$F_T^t \cdot \delta D_T = (F_I^t - F_R^t \cdot C_{TW}) \cdot \delta D_W$$

Therefore:

$$F_W = F_I - C_{TW}^t \cdot F_R \tag{15}$$

To obtain the W-form of the stiffness matrix and initial forces, F_I and F_R in eq. (15) are substituted from eqs. (10):

$$F_W = (K_{II} - C_{TW}^t \cdot K_{RI}) \cdot D_W + (K_{IR} - C_{TW}^t \cdot K_{RR}) \cdot D_R + F_I^o - C_{TW}^t \cdot F_R^o$$

Using eq. (13) for D_R:

$$F_W = K_W \cdot D_W + F_W^o \tag{16a}$$

where

$$K_W = K_{II} - C_{TW}^t \cdot K_{RI} - K_{IR} \cdot C_{TW} + C_{TW}^t \cdot K_{RR} \cdot C_{TW} \tag{16b}$$

$$F_W^o = F_I^o - C_{TW}^t \cdot F_R^o + (K_{IR} - C_{TW}^t \cdot K_{RR}) \cdot D_R^* \tag{16c}$$

Eqs. (16) give the W representation for the composite structure. Once the problem is solved, that is the displacements D_W are obtained, the redundant displacements D_R are given by eq. (13), and the T-form is obtained. Then eqs. (2) and (1) give the displacements and forces in the primitive representation.

In the case where no virtual work is done by the redundant degrees of freedom, i.e.:

$$F_R^t \cdot \delta D_R = 0$$

from eq. (14):

$$F_W = F_I$$

Then, from eq. (15):

$$C_{TW}^t \cdot F_R = 0$$

From (10.b) and (13):

$$C_{TW}^t \cdot (K_{RI} - K_{RR} \cdot C_{TW}) = 0$$

so:

$$C_{TW}^t \cdot K_{RI} = C_{TW}^t \cdot K_{RR} \cdot C_{TW}$$

Substituting in eqs. (16):

$$K_W = K_{II} - K_{IR} \cdot C_{TW}$$

$$F_W^\circ = F_I^\circ - K_{IR} \cdot D_R^*$$

which is Friedrich's result, valid only in the case where no virtual work is done by the redundant degrees of freedom.

2.2 Stiffness of a pellet and a cladding section.

The stiffness matrix and initial forces of a cladding section, satisfying:

$$F = K \cdot D + F^\circ$$

are calculated using thin shell theory.

Figure 1 shows a cladding section of mean radius a, thickness h and height l. No axial displacements are allowed in the lower end; the degrees of freedom (displacements and rotations) considered in the analysis are shown in the figure.

For the evaluation of the initial forces F_o the following loads are considered: constant temperature T_o, and a temperature difference ΔT between the inner and outer surfaces.

If the radial forces F_1 and F_4, axial force F_2 and bending moments F_3 and F_5 are defined per unit circumferential length, a thin shell calculation (26) gives the following stiffness matrix:

$$K = \begin{pmatrix} \frac{Eh}{a^2\beta} & \nu\frac{Eh}{\beta l a} & \frac{Eh}{2a^2\beta^2} & 0 & 0 \\ \nu\frac{Eh}{\beta l a} & E\frac{h}{l} & \nu\frac{Eh}{2al\beta^2} & \nu\frac{Eh}{a\beta l} & -\frac{\nu Eh}{2al\beta^2} \\ \frac{Eh}{2a^2\beta^2} & \nu\frac{Eh}{2al\beta^2} & \frac{Eh}{2a^2\beta^3} & 0 & 0 \\ 0 & \nu\frac{Eh}{a\beta l} & 0 & \frac{Eh}{a^2\beta} & -\frac{Eh}{2a^2\beta^2} \\ 0 & -\frac{\nu Eh}{2al\beta^2} & 0 & -\frac{Eh}{2a^2\beta^2} & \frac{Eh}{2a^2\beta^3} \end{pmatrix}$$

where E is the Young modulus, ν the Poisson ratio and

$$\beta = \left[\frac{3\,(1-\nu^2)}{a^2\,h^2}\right]^{1/4}$$

Higher order terms in $(\beta l)^{-1}$ have been neglected, as for typical fuel rod dimensions (l being the pellet height):

$a = 5.26$ mm

$l = 11.18$ mm $(l/d = 1)$

$\nu = .253$

is:

$\beta = 1.439$ mm

The initial forces due to a temperature difference ΔT between the cladding inner and outer radii are:

$$F^{o}_{\Delta T} = \frac{E\alpha h^2 \Delta T}{12\,(1-\nu)} \begin{bmatrix} 0 \\ 0 \\ 1 \\ 0 \\ -1 \end{bmatrix}$$

where α is the coefficient of linear thermal expansion, and those due to a uniform temperature increment T_o are:

$$F^{o}_{T_o} = E h \alpha T_o \begin{bmatrix} \dfrac{-(1+\nu)}{a\beta} \\ -\left(1+\dfrac{2\nu}{\beta l}\right) \\ \dfrac{-(1+\nu)}{2a\beta^2} \\ \dfrac{-(1+\nu)}{a\beta} \\ \dfrac{1+\nu}{2a\beta^2} \end{bmatrix}$$

The stiffness matrix and initial forces for the pellet have been calculated using the finite element codes ADINA (27), SAP4 (28) and ELASTEF (29). A linear thermoelastic behavior is assumed, with uniform values for the elastic modulii, thermal lineal expansion and heat conductivity.

The degrees of freedom taken into account are shown in Fig. 2. Points A, where the pellet contacts the next one, are taken as fixed (no axial or radial displacement); assembling the pellet stack will be done by the method described in 2.1.

The linearity of the problem allows to obtain the initial forces due to a linear heat generating rate q and surface temperature T_S from the initial forces calculated for unitary values of q and T_S. Heat generation is assumed to be uniform in the pellet (neither flux depression nor end-effects are considered). This leads to a parabolic tem perature distribution:

$$T(r) = \frac{q}{4\pi k}\left(1 - \frac{r^2}{R^2}\right)$$

where q is the increment of linear power during the ramp; k the average thermal conductivity of the pellet; R the pellet radius.

The concentrated axial force F_1 (Fig. 2) in the case of flat-ended pellets is rather artificial, as two elastic bodies in point contact (two pellets in this case) will deform and develop a contact surface. This problem was solved by Hertz (30). Let two elastic bodies contact at points where their radii of curvature are ρ_1 and ρ_2, with a contact force F. Then, assuming a parabolic distribution for the contact pressure, the radius r_c of the circular contact area will be:

$$r_c = \left(\frac{3\,F\rho}{4\,E}\right)^{1/3}$$

where:

$$\frac{1}{\rho} = \frac{1}{\rho_1} + \frac{1}{\rho_2}$$

$$\frac{1}{E} = \frac{1-\nu_1^2}{E_1} + \frac{1-\nu_2^2}{E_2}$$

For two pellets in contact $E_1 = E_2 = E$; $\nu_1 = \nu_2 = \nu$; $\rho_1 = \rho_2 = \rho$ is the radius of curvature due to thermal hourglassing. Table I gives for different power levels as cal culated by the ADINA finite element code.

A LHGR of 30 kw/m is taken as representative of rod conditions. Then ρ = 263.2 mm, and with ν = 0.3:

$$r_c = 5.641\ (F/E)^{1/3}$$

Figure 3 shows parametrically the contact radius r_c as a function of axial compressive force F and fuel Young modulus E. A value of r_c = 1/3 R was adopted, as representative of the order of magnitude of compressive forces found in calculations; geometric non-linearities due to the dependence of r_c on the axial compressive load are avoided in this way.

2.3 Representation of a fuel rod.

The method presented in section 2.1 is repeatedly applied to obtain a representation of a fuel rod consisting of n pellets. Pellet-clad contact is modeled following the ideas of Liu et al (32).

The stiffness matrix and initial forces for each pellet, and for the n sections in which the cladding is divided, are obtained as shown in 2.2. This gives the P-form for each pellet and cladding section. In order to set convenient boundary conditions, two additional cladding sections are introduced: one at the top, and the other at the bottom of the pellet stack.

The linear heat generating rate, pellet and cladding surface temperatures and pellet-cladding friction coefficients can have arbitrary values for each pellet and corresponding cladding section. Also each pellet may or may not be in contact with the cladding.

Three steps in the assembling process to obtain the representation of the fuel rod are presented here:

a) assembling the first pellet/cladding section to the cladding section 0 at the bottom of the stack.

b) assembling pellet/cladding section i^{th} ($i = 2, 3, .. n$) to the first i-1 pellet/cladding sections.

c) assembling cladding section n+1 at the top of the cladding to the n pellet/cladding sections.

In all cases the following conditions are imposed:

- Equal radial displacements of pellet and cladding at the contact points.
- Continuity of radial displacements and rotations of the cladding.

- Radial equilibrium of forces at the contact points.
- Equilibrium of moments acting on the cladding.
- Axial equilibrium of forces in both pellet and cladding.
- Friction relations. When pellet and cladding are stuck at the contact points, equal axial displacements are imposed. When sliding occurs, the tangential force is made equal to the friction coefficient times the normal force; different cases may happen regarding the direction of the tangential force, as will be discussed later.

In steps a) and c) additional boundary conditions are established at the cladding sections at the top and bottom of the rod. Zero radial displacements and rotation of the cladding are imposed there, as a way of simulating approximately rigid end-caps.

During the assembling process, the addition of pellet-cladding section i, with 10 degrees of freedom (Figs. 1 and 2), to the first i-1 sections, leads to 10 redundancy conditions. Therefore, matrix M_R in eq. 11.b is 10 x 10, and the inversion of a 10 x 10 matrix is required for each pellet. This makes computer times low. On the other side, iterations are necessary until a consistent system of relative displacements at contact points, directions and values of friction forces, and sliding or stucking of each pellet, is reached.

The linearity of the model allows to treat any axial distribution of linear power increase during the ramp. Also, each pellet may or may not contact the cladding.

3. DISPLACEMENT OF A SINGLE PELLET RELATIVE TO THE CLADDING.

In this section different possibilities of relative displacement of fuel and cladding will be analysed, as determined by friction effects.

The main fact to be reminded is that, when no interaction occurs between fuel and cladding, the axial expansion of the pellet stack during a power-up ramp is larger than the axial expansion of the cladding (due to its larger thermal expansion). Therefore, the consideration of friction effects between contacting pellets and the cladding can never lead to a situation where the total pellet stack expands axially less than the cladding.

Figure 4 shows three of the possibilities for the relative displacements at any pellet. Fig. 4-a despicts a "completely stuck situation": due to friction, pellet and cladding are stuck at the contact points, and the axial displacements of pellets and cladding are equal. In this case, forces and displacements referred to the pellet midplane are symmetric to the pellet midplane. This situation is attained for a given value of the axial compressive force F_Z acting on the pellet.

If the tangential friction force F_T needed to attain this situation is larger than the friction coefficient μ times the normal force F_N, the pellet will slide with respect to the cladding. The situation will be the one despicted in Fig. 4-b, which is again symmetric to the pellet midplane.

The direction shown for the friction forces $\mu \cdot |F_N|$ is compatible with a final deformed state where, at the upper pellet face, the contact point in the cladding has moved upwards with respect to the pellet; at the bottom, the opposite situation must occur. Other sliding situations are possible, with opposite directions for the friction forces.

Figure 4-c shows a situation of "non symmetric sliding". Pellets in the upper region of the stack are pushed upwards by the larger thermal expansion of the other pellets; consequently, the tangential friction forces at both pellet ends point downwards, i.e. opposite to the direction of relative displacement of the contacting surfaces. This situation is non-symmetric to the pellet midplane, and results in a build-up of axial compressive forces from pellet to pellet, as shown in Fig. 4-c.

The completely stuck situation.

In Fig. 4-a this situation was shown; pellet and cladding axial deformations are equal, and both bodies are stuck due to friction at the contact points. This situation corresponds to the one described in 1 and $1^1/_2$ dimensional fuel rod codes in cases where, after pellet-clad contact, equal axial displacements of fuel and clad, under the generalized plane strain hypothesis, are imposed.

This situation can be very easily modelled, as the symmetry to the pellet midplane allows to restrict the analysis to a single pellet and cladding section. The ratio $e = E_f/E_c$ of the Young modulii of fuel and cladding is taken as a parameter.

Tabla II gives the geometric data for the cladding and the six pellet shapes studied; Table III shows the material properties assumed for UO_2 and Zry.

The calculations are made for a power-up ramp of 30 kw/m. In Fig. 5 the axial compressive force on the pellet (and axial tensile force on the cladding) required to obtain the completely stuck situation is plotted as a function of e. To clarify figures, the maximum value of e (2.22) corresponds (31) to a pellet average temperature of 1160°C and 95% TD, and to a Young modulus for the cladding E_{Zry} = 76700 MPa.

Figure 6 shows the radial deformation of the cladding at the contact points. Basic qualitative facts agree with the experimental evidence on the effect of pellet shape (20-24): dished pellets produce larger ridges than flat-ended ones; increasing the L/D ratio increases ridging, but the effect is much more important for dished pellets.

An "effective" friction coefficient μ_{eff} is defined as the absolute value of the ratio between the tangential friction force and the normal force at the contact points. μ_{eff} is shown in Fig. 7. In all cases, μ_{eff} becomes zero for a certain value of the ratio e of Young modulii. At that point the tangential force becomes zero, and then changes direction. As shown in Fig. 7, for "hard" pellets (large e) the friction forces are tensile on the pellet, i.e. they must counteract the compression axial force in order to attain a completely stuck situation. For a given value of e, if the friction coefficient μ between pellet and cladding is smaller than the effective μ_{eff}:

$$\mu < \mu_{eff}$$

Then
$$|F_T| > \mu |F_N|$$

and sliding will occur. Therefore, Fig. 7 gives also the values of μ for which a completely stuck situation is possible, i.e. $\mu \geq \mu_{eff}$. It can be seen from the figure that, for reasonable values of μ ($\leqslant 0.50$), the range of values of e for which complete stucking is possible is much wider for dished than for flat-ended pellets.

This analysis will prove to be very helpful in reducing the number of iterations when a whole rod is analysed.

4. STUDY OF A FUEL ROD

A pellet stack 500 mm long was considered. Depending on the L/D ratio of the pellets (see Table II), it will consist of 30 pellets with L/D = 1.7, or 51 pellets with L/D = 1, or 103 pellets with L/D = 0.5.

In case I the "completely stuck situation" can be reached by some pellets in the stack. A friction coefficient $\mu = 0.25$ and a ratio of Young modulii $e = 0.78$ are adopted (see Fig. 7).

In Fig. 8 the cladding radial displacement $\underline{d}$ at the pellet interfaces is plotted along the rod, for a constant (no axial dependence) power-up ramp of 30 kw/m. For the sake of clarity $\underline{d}$ is plotted as a continuous function of the axial coordinate, but actually it is only defined at the pellet interfaces, i.e. at 31, 52 or 104 points depending on the L/D ratio.

On each curve, an arrow indicates the boundary between sliding pellets (upper region of the stack), and "completely stuck" pellets. Being the power constant, all stuck pellets behave the same, and $\underline{d}$ is independent on the axial position.

For all pellet shapes, there is a maximum on $\underline{d}$ for the upper pellet interface, reflecting the influence of the boundary conditions imposed. In the rest of the sliding region, flat-ended and dished pellets behave the opposite: for dished pellets, the radial displacement of the cladding increases from pellet to pellet, while for flat-ended ones it diminishes.

Figure 8 also shows the axial elongation ΔZ of the pellet stack and the cladding. While the total stuck situation prevails, both elongations are the same; in the upper part of the rod, where sliding occurs, the fuel elongation becomes increasingly larger than the cladding elongation.

Figure 9 gives the reason for this behavior. There, the axial compressive force on each pellet (opposite to the axial tensile force on the cladding) is plotted as a function of axial position; again continuous curves were drawn for the sake of clearity. As we move down along the rod, the compressive force increases for all pellet shapes in the region of "non symmetric sliding" (Fig. 4-c), and remains constant once the stuck situation is reached. The effect of the axial compressive force is schematically shown in Fig. 10: for a dished pellet it adds to the thermal hourglassing, while for a dished one it counterbalances it. As a result, the build-up of compressive axial forces due to friction effects in the sliding pellets results in increasing cladding radial deformation for dished pellets, and in decreasing d for flat-ended ones, as shown in Fig. 8.

A qualitative picture of the fuel rod behavior can now be drawn; similar behavior will be found in the other cases to be analysed. At the bottom of the rod, pellets are either stuck or symmetrically sliding with respect to the cladding. Those situations require considerable axial forces compressing the pellets; compare the magnitude of the forces shown in Fig. 9, to a typical gas-pressure induced force on a pellet, of the order of 400 N for a pressure of 50 atmospheres. Those compressive forces are build-up from the friction forces at the top of the column, where (see Fig. 4-c) pellets slide upwards with respect to the cladding; once a symmetric situation is reached, either with sliding or stuck pellets, the build-up of compressive forces end.

The qualitative differences between pellet shapes agree with the experimental evidence (20-24): pellet dishing increases cladding "ridging"; increasing L/D ratio also increases "ridging", and this effect is much more important for dished pellets than for flat-ended ones (see Fig. 8).

Another interesting effect is that the extension of the region of sliding pellets is larger the larger the L/D ratio. In other words, what is similar is the number of sliding pellets. This is due to the discrete nature of a pellet stack, and to the fact that the build-up of axial compressive forces per pellet, due to friction forces, is relatively independent of pellet length.

In Case II, the axial power distribution is changed; values of μ and e are the same as in Case I.

Two linear axial distributions of the increase of power during the ramp are considered, both of them between 22 kw/m and 30 kw/m. In one case, Fig. 11, the power is increased 22 kw/m at the top of the stack, and 30 kw/m at the bottom; in the second case, Fig. 12, it increases by 30 kw/m at the top, and by 22 kw/m at the bottom of the stack.

Figures 11 and 12 show the radial displacement of the cladding at the pellet interfaces in both cases.

The displacement <u>d</u> follows the change of power in the region of stuck pellets; Fig. 13 shows, for flat-ended pellets with L/D = 1 (the behavior is similar for other pellet shapes), the symmetry of cladding deformation in the region of stuck pellets. On the other side, the behavior is very different for the sliding pellets at the top of the stack. Predicted ridging for flat-ended pellets is larger when the maximum power is at the top of the rod. For dished pellets, the effect of compressive axial forces discussed earlier leads to a situation (Fig. 12) where pellets generating higher power induce smaller radial deformations in the cladding.

Figure 14 shows axial displacements per unit length in the constant power case (Case I). Figure 14-a shows the axial displacement of the cladding as a function of the L/D ratio. Curves are drawn continuous, but actually only three points have been calculated (L/D = 0.5; 1; 1.7). Axial deformations are larger for flat-ended pellets than for dished ones, except for the long, L/D = 1.7 case. Cladding axial strain increases with L/D, especially for dished pellets; this agrees with the usually observed behavior (21-23).

Figure 14-b plots the axial displacement per unit length of the pellet stack. The dependence on pellet shape is similar to the one predicted for cladding axial strains.

The behavior shown in Cases I and II does not depend on having stuck pellets. In Case III, a constant power-up ramp of 30 kw/m is simulated; μ is adopted to be 0.10 and e = 1.557.

Figure 15 shows the cladding radial displacement at pellet interfaces. Due to a smaller value of the friction coefficient, the region of "non symmetric sliding" is much larger than in the previous case; in the rest of the rod, symmetric sliding (similar to the one shown in Fig. 4-b) exists. Figure 16 shows the much slower build-up of axial compressive forces due to the smaller value of μ.

Increasing the value of μ to 0.25 and 0.50 keeping the same ratio e of Young modulii, as shown in Figs. 17-a and 17-b, reproduces the same kind of behavior. The larger the value of μ, the larger the build-up of compressive axial forces in the sliding pellets at the top, resulting in a decreasing number of "non symmetric" sliding pellets.

Figures 18 and 19 show axial displacements per unit length for both cladding and pellet stack, for the cases $\mu = 0.10$ and $\mu = 0.50$. The model predicts a rather small dependence of axial strains on the friction coefficient in these cases. It can also be noted that, for flat-ended pellets, the dependeпe of axial strains on L/D is small and can even be opposite compared to dished pellets; this behavior has been found in some cases (Ref. 23, Table V, test DME-143).

Comments on fuel axial elongation.

We return to the axial displacement per unit length of the pellet stack in Case I, that was shown in Fig. 13-b. In Fig. 20 the same displacements are compared to the axial displacement per unit length of a pellet due only to the thermal hourglassing effect, as calculated by the SAP-4 code.

The thermal elongation is very different for flat-ended and dished pellets. In the first case, axial strains fall rapidly as L/D increases, while for dished pellets there is a small increment of $\Delta L/L$ as L/D increases. Figure 21 allows to understand the situation. The deformed shape, due to thermal hourglassing alone, of the 6 pellet shapes is shown; also the axial thermal strain for an infinite cylinder (plain strain limit) is shown. $\Delta L/L$ is given by the displacement of the pellet centerline for flat-ended pellets, and by the displacement of the pellet shoulder for the dished ones. For flat ended pellets, end-effects give axial deformations larger than the plain-strain value, but the difference between actual and plain strain axial deformation (i.e., the end-effect) is mainly independent of L/D. In other words, there is a central zone in the pellet under a plain-strain state, with axial displacements linear with L, and a local deformacion on the surface rather independent of L (specially for L/D = 1 and 1.7). When the axial displacement per unit length is considered, the contribution of the local deformation becomes smaller as L increases, and the behavior is the one shown in Fig. 20.

For dished pellets, end-effects are such that for longer pellets, axial displacements of the pellet shoulder becomes smaller than the plain strain value; this is a Poisson effect, due to the eccentric position of the pellet shoulder. This gives a small increment of $\Delta L/L$ as L increases, as shown in Fig. 20.

A striking fact is the qualitative difference of dependence of purely thermal and total axial strains on the L/D ratio. This shows the importance of including good estimates of the forces when modeling pellet clad interaction.

5. CONCLUSIONS

This study allows to draw several conclusions:

1.- Even a simplified, linear thermoelastic analysis of pellet-cladding mechanical interaction, allows to explain the main qualitative facts of the behavior of different pellet shapes.

2.- In order to attain such agreement with experimental evidence, the effect of axial forces must be taken into account. For instance, thermal hourglassing alone would give no measurable differences in cladding ridging between flat-ended and dished pellets.

The evaluation of the order of magnitude of these axial forces implies, specially when pellets and cladding are sliding, some kind of analysis of the whole stack.

3.- Thermal hourglassing alone without consideration of the forces acting on the contacting pellets and cladding, is also unable of explaining the dependence of axial strains on the L/D ratio of the pellets.

4.- The value of the friction coefficient between pellets and cladding does not seem to have a large influence on the predictions of this model. Its value will determine mainly the number of pellets sliding with respect to the cladding at the top of the rod.

5.- The assumption of symmetric deformations of pellet and cladding respect to the pellet midplane is not valid for the first pellets in the stack, where sliding occurs. Depending on the power axial distribution and pellet shape, the larger cladding strains may be on that region.

ACKNOWLEDGEMENTS

Finantial support for the runs of the ADINA code was provided by Entropy Limited, Lincoln, Mass., USA. Partial funding for this work was provided by the Organization of American States.

We wish to thank G. Sánchez Sarmiento for assistance in running the ELASTEF code, and Eduardo Savino for helpful discussions and critical reading of the manuscript.

REFERENCES

1. S. Levy, J.P.D. Wilkinson. Trans. 2nd SMIRT Conf. Vol.I part C-D, D1/5 (1973).

2. P.N.R. Keegstra, J.L. Head, A. Alujevič.Trans. 2nd SMIRT Conf., Vol.I, part C-D, C3/3 (1973).

3. Y.R. Rashid. Nucl. Eng. and Design 29 (1974) p.22.

4. M. Hsu, W. Lee. EPRI-277, final report (1975).

5. F.E. Bard, V.W. Watwood. HEDL-TME 75-89 (1975).

6. K. Muja, M. Hashimoto, Y. Ando, Trans. 3rd SMIRT Conf. Vol. I, part C-D, C3/8 (1975).

7. M. Das, R.S. Rustagi. Trans. 4th SMIRT Conf. Vol. C, C3/11 (1977).

8. J.J.M. Too, G.L. Rigby, H. Tamm. Trans. 4th SMIRT Conf. Vol. D, D1/8 (1977).

9. G.P. Engelman. CDAP-TR-78-041 (1978).

10. R.S. Darling, I.B. Fiero, M.E. Scott. Trans. 5th SMIRT Conf., Vol. D, D2/8 (1979).

11. M. Kinoshita, M. Ichikawa. Nucl. Eng. and Design 56 (1980) p. 49.

12. Y. Iwano. Nucl. Eng. and Design 56 (1980) p. 41.

13. A. Strasser, H. Heckermann, N. Hoppe. EPRI Sponsored Specialists Meeting, Tucson, Arizona (1977).

14. K. Lassmann. Nucl. Eng. and Design 45 (1978) p.325-342.

15. H. Fenech, H.M. Guerón. Nucl. Applic. 3 (1967) p. 406.

16. R.A. Valentin, J.J. Carey. Nucl. Eng. and Design 12 (1970) p. 277.

17. J. Veeder. AECL 2660.

18. J.R. Matthews. Advances in Nuclear Science and Engineering, Vol. 6 (1972) p. 65. Academic Press, New York.

19. J.J. Carey, R.A. Valentin. Trans. 1st SMIRT Conf., Vol. 2, part C, C3/2 (1971).

20. W.J. Bailey, C.L. Wilson, L.J. Mac Gowan, P.J. Pankaskie. COO-4066-2/PNL-2488/UC-78 (1977).

21. S. Aas. Nucl. Eng. and Design 21 (1972) p.237.

22. T.J. Carter - AECL 5978 (1977)

23. T.J. Carter. Nucl. Technol. 45 (1979) p. 166.

24. J.F. Whatham. Nucl. Eng. and Design 26 (1974) p.423.

25. C.M. Friedrich. WAPD-TM-1140.

26. S. Timoshenko, S. Woinowsky-Krieger. "Theory of plates and shells", McGraw Hill, New York (1959).

27. K.J. Bathe. ADINA User's Manual, MIT, N°82448-1 (Revised May 1977).

28. K.J. Bathe, E.L. Wilson, F.E. Peterson: SAPIV: A structural analysis program for static and dynamic response of linear systems. Report to N.S.F., College of Engineering, University of California, Berkeley, Cal., USA (1974).

29. G. Sánchez Sarmiento. CNEA-NT 21/80 (1980).

30. H. Hertz. "Miscellaneous Papers", Macmillan, New York (1896), p. 146.

31. MATPRO. Version 09. Tree-Nureg-1005 (1976).

32. Y.Y. Liu, J.E. Meyer and A.S. Argon, Trans. 5th SMIRT Conf., Vol. D, D3/5 (1977).

Table I

Radius of curvature at the center of the pellet end-face due to thermal hourglassing

q w/m	ρ mm	ρ/R
20	394.9	81
30	263.2	54
40	197.4	40
45	175.5	36

Pellet radius R = 4.8768 mm

Table II

Pellet and cladding geometrical data

Type	Dishing volume %	Radius mm	Height mm	Dishing radius* mm	Dishing height mm	L/D
D 0.5	2	4.8768	4.8768	3.752	.1128	0.5
D 1	2	4.8768	9.7536	3.752	.2253	1
D 1.7	2	4.8768	16.708	3.752	.3851	1.7
FE 0.5	-	4.8768	4.8768	-	-	0.5
FE 1	-	4.8768	9.7536	-	-	1
FE 1.7	-	4.8768	16.708	-	-	1.7

* Spherical dishing was considered.

Table III

Material properties

Material	ν	α 1/°C	k kw/m °C
UO_2	0.30	$.1086 \times 10^{-4}$	.002843
Zry	0.253	$.6721 \times 10^{-5}$	.0165

FIGURE CAPTIONS

Fig. 1 : Cladding section corresponding to one pellet. The degrees of freedom considered in the analysis are shown.

Fig. 2 : Degrees of freedom considered for a pellet. In the case of dished pellets, axial forces (d.o.f.#1) are transmitted from pellet to pellet through the pellet shoulder, as indicated.

Fig. 3 : Lines of equal contact area for flat-ended pellets in contact. F is the axial compressive force transmitted through the contact area; E the pellet Young modulus. The radius r_c of the circular contact area is given as a fraction of the radius R of the pellet.

Fig. 4 : Some possibilities of pellet-cladding relative displacements. In all cases the reference state is drawn in full lines, and the deformed one in dot-lines. Axial forces on the cladding (not shown) are opposite to the ones on the pellet.

4a) Completely stuck situation. Axial displacements $\overline{11}'$ of fuel and $\overline{33}'$ are equal; there is no sliding at the contact points. The direction shown for the tangential friction forces F_T is arbitrary.

4b) Symmetric sliding: axial deformations of fuel and cladding are different. The direction of F_T is consistent with a larger axial expansion of the cladding as compared to the pellet at the contact points.

4c) Non symmetric sliding: the pellet as a whole, pushed by the thermal expansion of the rest of the stack, slides upwards respect to the cladding. Both tangential friction forces point downwards, resulting on a buil-up of the axial compressive force on the following pellet.

Fig. 5 : Completely stuck situation. Axial compressive force F_1 on the pellet as a function of the ratio e of Young modulii of fuel and cladding. Values for a power-up ramp of 30 kw/m. The L/D ratio is marked on each curve.

Fig. 6 : Completely stuck situation. Radial displacements d of the cladding at the pellet interface as a function of the ratio e of Young modulii. Values for a power-up ramp of 30 kw/m. On each curve the L/D ratio is indicated.

Fig. 7 : Completely stuck situation. Absolute value of the ratio between tangential and normal forces at the contact points, μ_{eff}, as a function of e. The direction of the tangential friction forces is shown schematically. If the friction coefficient μ falls in region A, the completely stuck situation is forbidden; in region B it is allowed. The cases to be analysed are marked. Numbers on each curve correspond to the L/D

ratio.

Fig. 8 : 500 mm long rod. Radial displacement d of the cladding at pellet interfaces as a function of axial position on the rod and axial elongation ΔZ of fuel and cladding. Case I: power up ramp of 30 kw/m, no axial distribution; $\mu = 0.25$; $e = 0.778$. Arrows mark the beginning of non-symmetric sliding. Numbers on each curve indicate the L/D ratio.

Fig. 9 : Axial distribution along the rod of the axial compressive force on each pellet. Case I.

Fig. 10 : Schematic representation of the deformation due to an axial compressive force acting on a flat-ended and on a dished pellet.

Fig. 11 : Case II. Cladding radial displacement d at the pellet interfaces for the power-up ramp shown in the figure. $\mu = 0.25$; $e = 0.78$

Fig. 12 : Case II. Cladding radial displacement d at pellet interfaces, for the plotted power-up ramp.

Fig. 13 : Comparison of the axial distribution of cladding radial displacement for the cases shown in Figs. 8, 11 and 12. Results for flat-ended pellets, with L/D = 1 are shown.

Fig, 14 : Case I (constant power). Axial displacement per unit length of the classing (Fig. 14 a) and the pellet column (Fig. 14 b), as a function of L/D.

Fig. 15 : Case III. Cladding radial displacement at the pellet interfaces for a constant power-up ramp of 30 kw/m. $\mu = 0.10$; $e = 1.557$. The L/D ratio is indicated on each curve.

Fig. 16 : Case III. Distribution along the column of the axial compressive force on each pellet. $\mu = 0.10$; $e = 1.557$. The L/D ratio is indicated on each case.

Fig. 17 : Case III. Cladding radial displacement at the pellet interfaces for a constant power-up ramp of 30 kw/m; $e = 1.557$.

17 a) $\mu = 0.25$ 17 b) $\mu = 0.50$

Fig. 18 : Case III. Axial displacement per unit length of the cladding (Fig. 18 a) and the pellet column (Fig. 18 b) as a function of the L/D ratio. Constant power-up ramp of 30 kw/m; $e = 1.557$; $\mu = 0.10$

Fig. 19 : Case III. Same as Fig. 18 for $\mu = 0.50$.

Fig. 20 : Case I. Constant power-up ramp of 30 kw/m; $e = 0.78$ $\mu = 0.25$. Axial displacement per unit length pf the pellet column. "Thermal" indicates the effect of thermal hourglassing alone; "Total" indicates the results of the present model.

Fig. 21 : Deformed shape of the pellet end-face due to thermal hourglassing for a power-up ramp of 1 kw/m. The six pellet shapes considered are shown; u_{∞} indicates,

for each L/D ratio, the axial displacement resulting from plane strain.

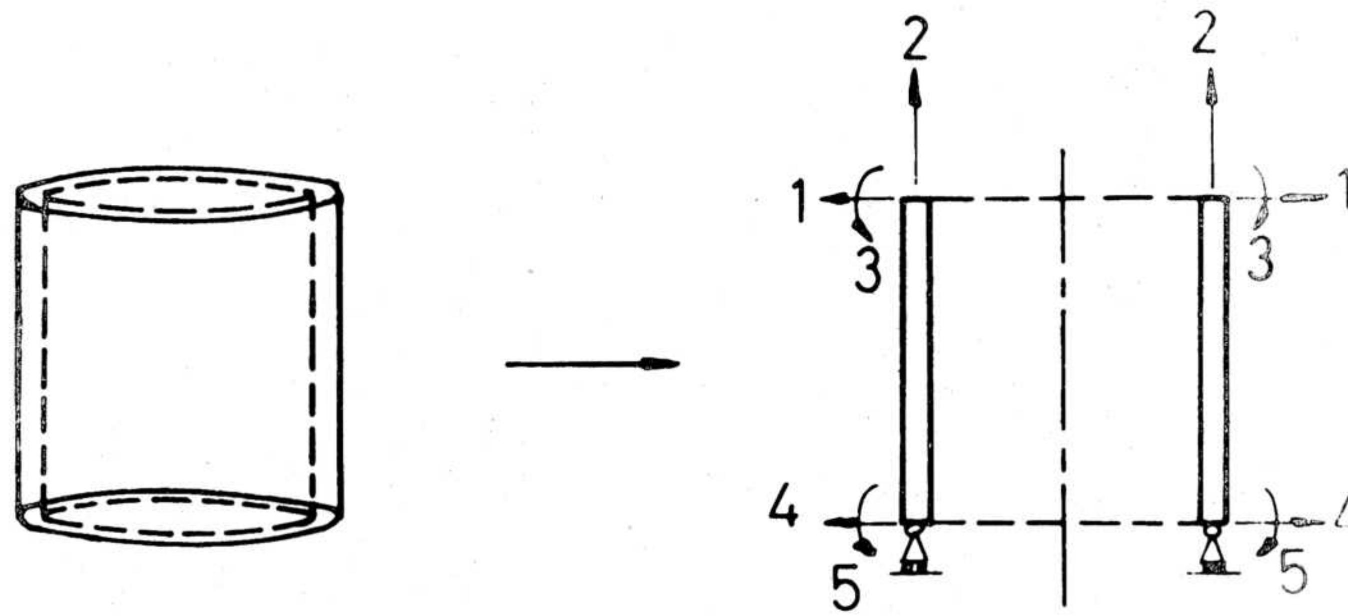

FIG. 1

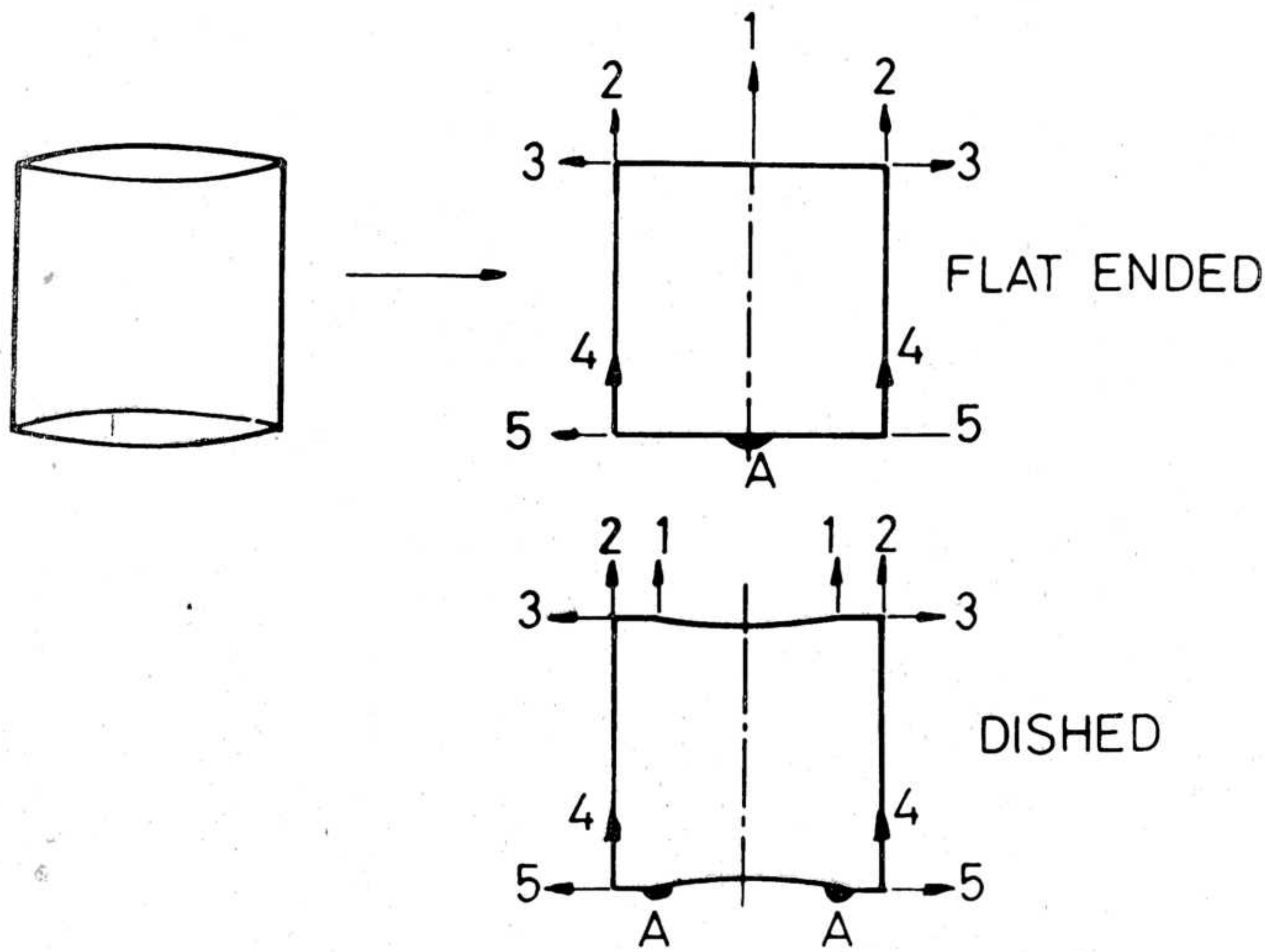

FIG. 2

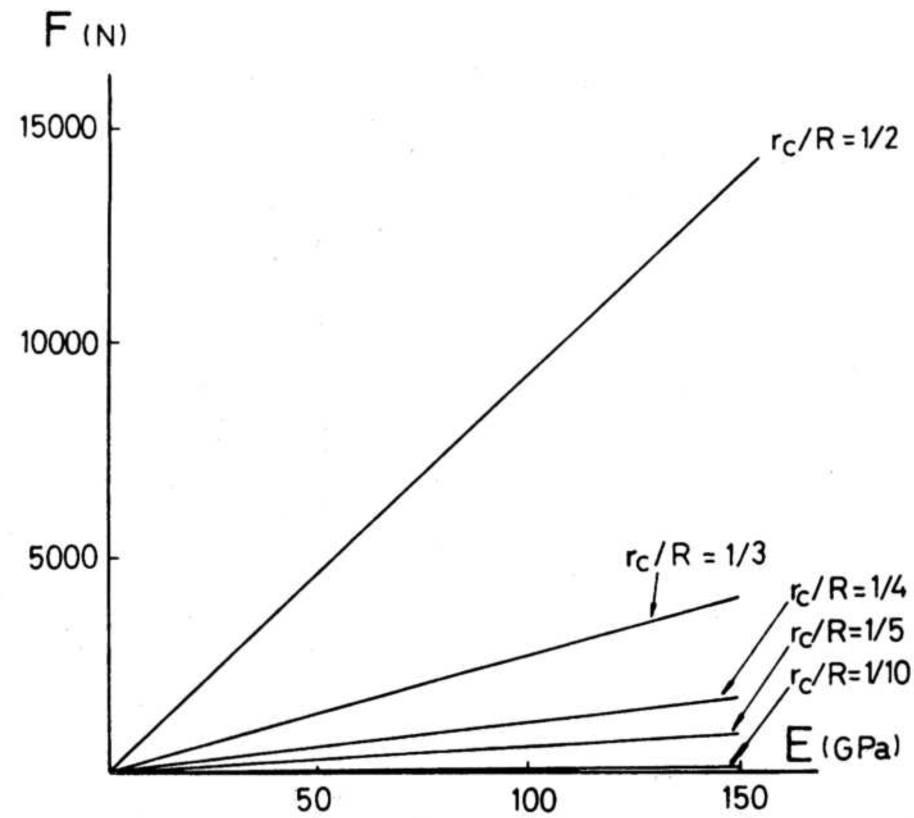
F (N)
15000
10000
5000
$r_c/R = 1/2$
$r_c/R = 1/3$
$r_c/R=1/4$
$r_c/R=1/5$
$r_c/R=1/10$
E (GPa)
50
100
150

FIG. 3

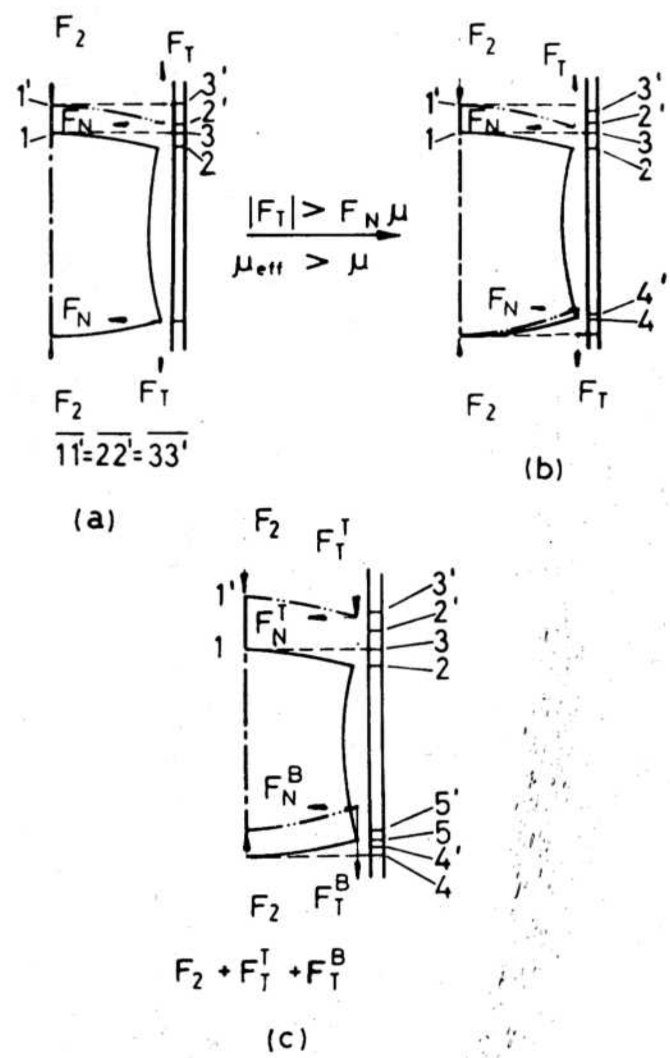
F_2
F_T
1'
1
F_N
3'
2'
3
2
$|F_T| > F_N\mu$
$\mu_{eff} > \mu$
4'
4
$\overline{11'}=\overline{22'}=\overline{33'}$
(a)
(b)
F_T^T
F_N^T
F_N^B
5'
5
F_T^B
$F_2 + F_T^T + F_T^B$
(c)

FIG. 4

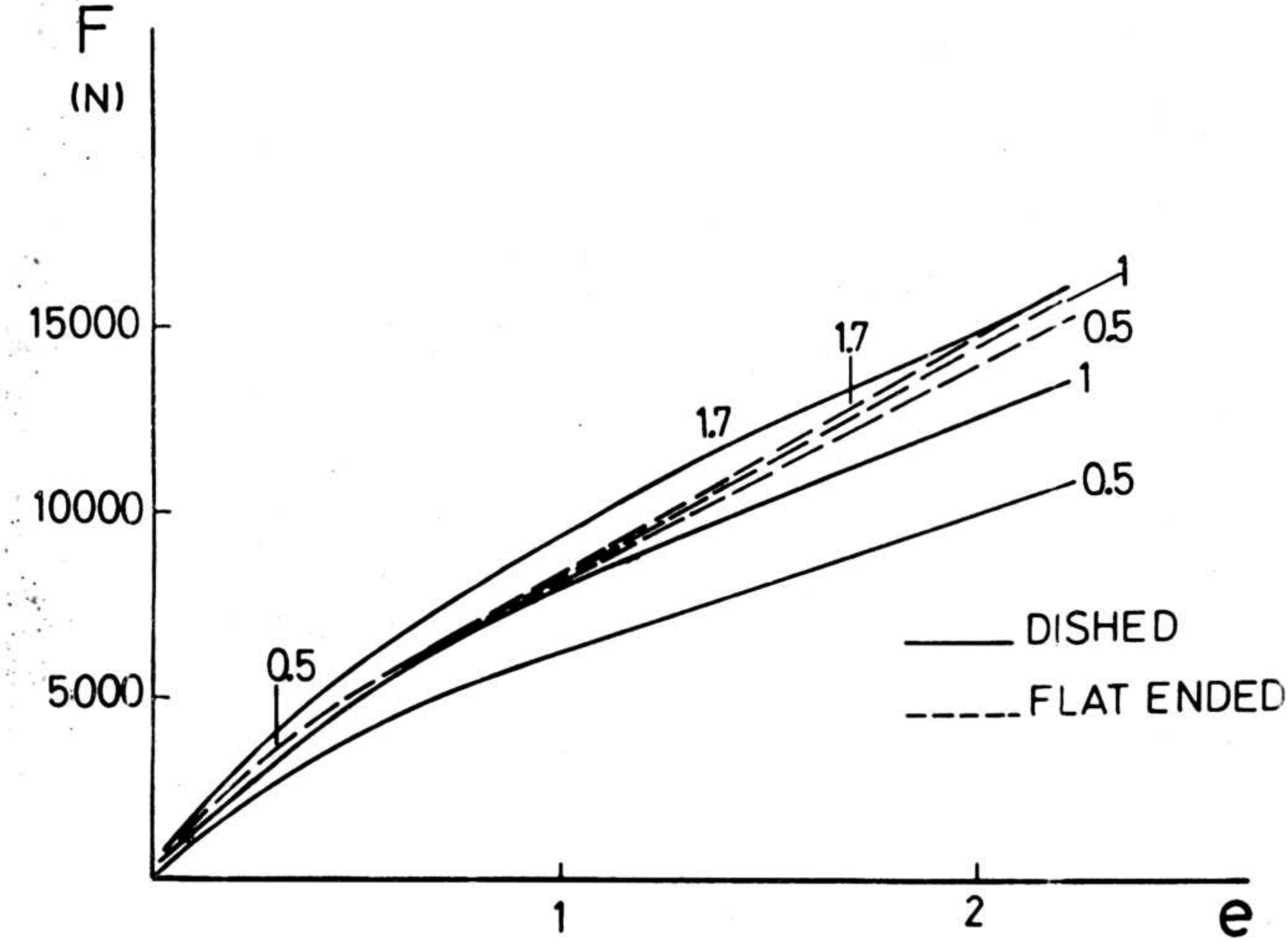
F
(N)
15000
10000
5000
1
2
e
1
0.5
1.7
1.7
1
0.5
0.5
DISHED
FLAT ENDED

FIG. 5

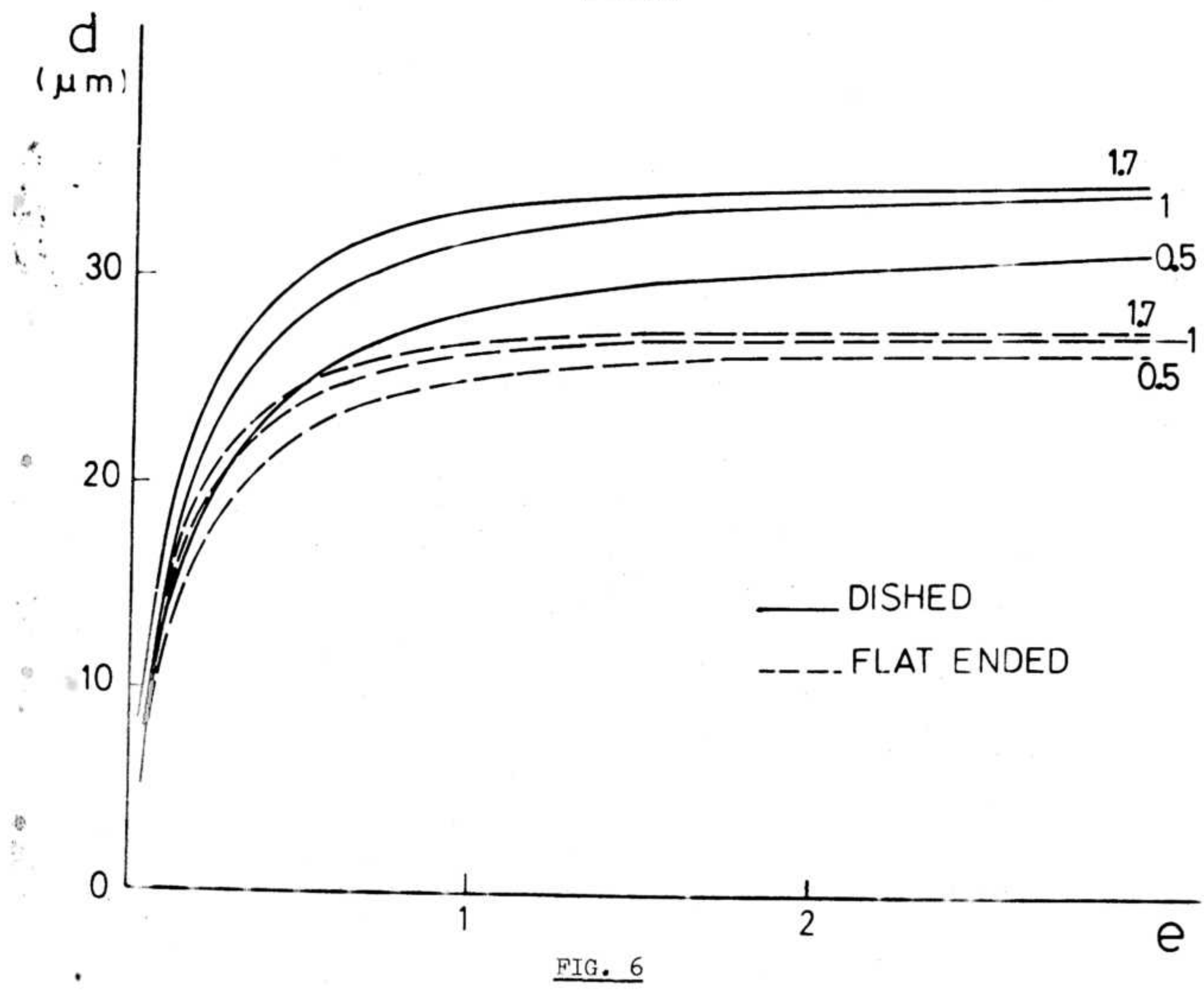
d
(μm)
30
20
10
0
1
2
e
1.7
1
0.5
1.7
1
0.5
DISHED
FLAT ENDED

FIG. 6

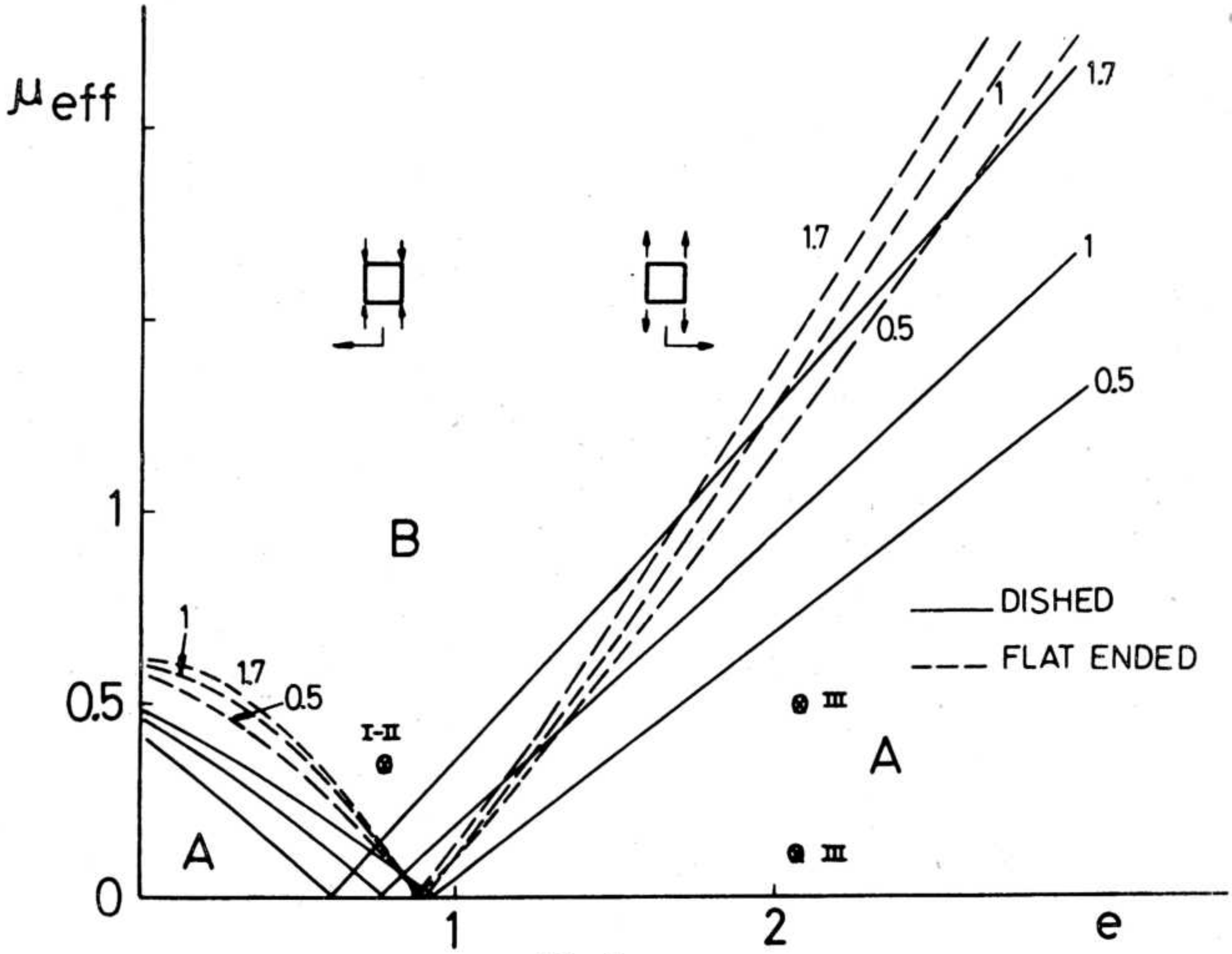

μeff
1
0.5
0
1
2
e
B
A
A
1.7
1
0.5
1.7
1
0.5
1
1.7
0.5
I-II
III
III
DISHED
FLAT ENDED

FIG. 7

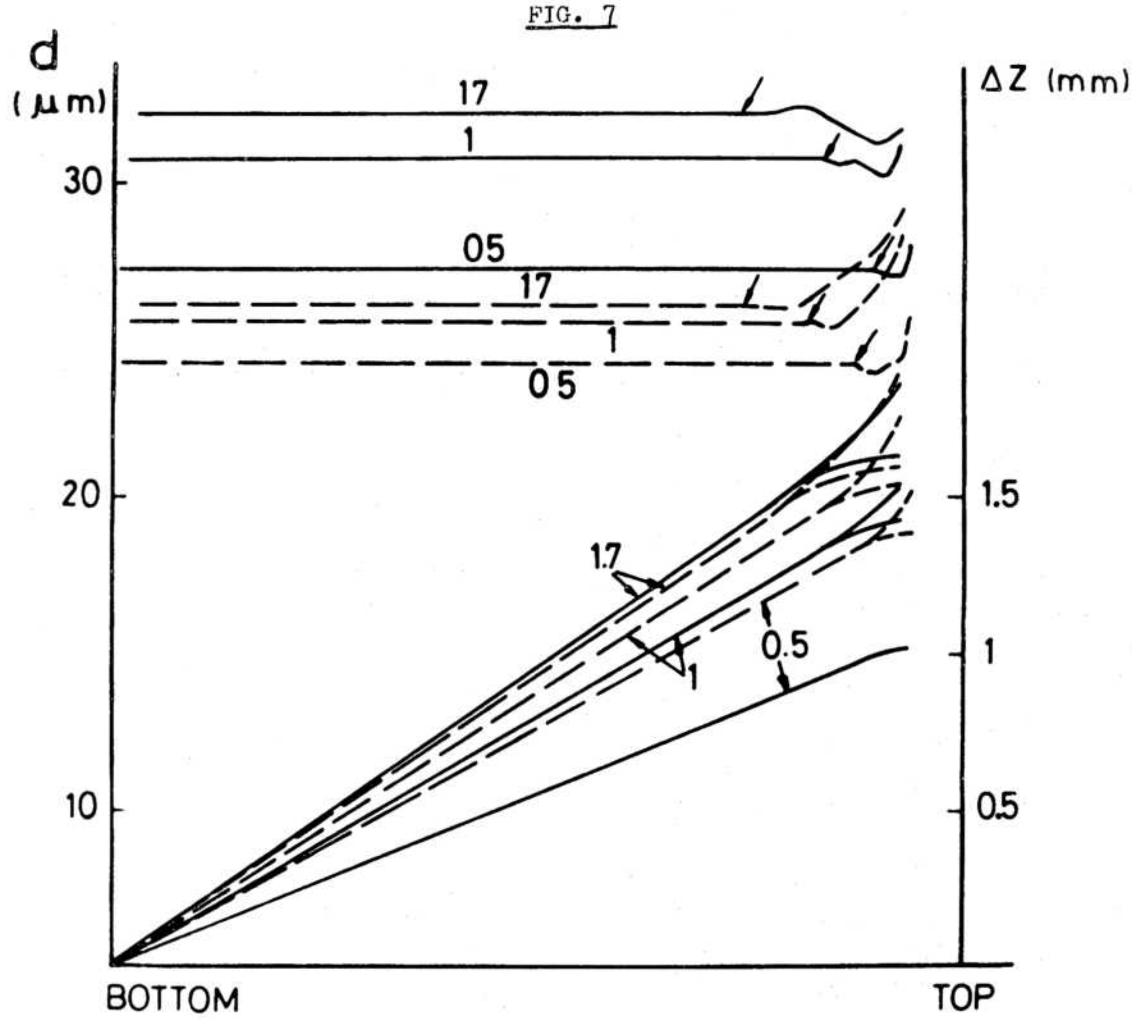

d
(μm)
30
20
10
ΔZ (mm)
1.5
1
0.5
17
1
05
17
1
05
1.7
1
0.5
BOTTOM
TOP

FIG. 8

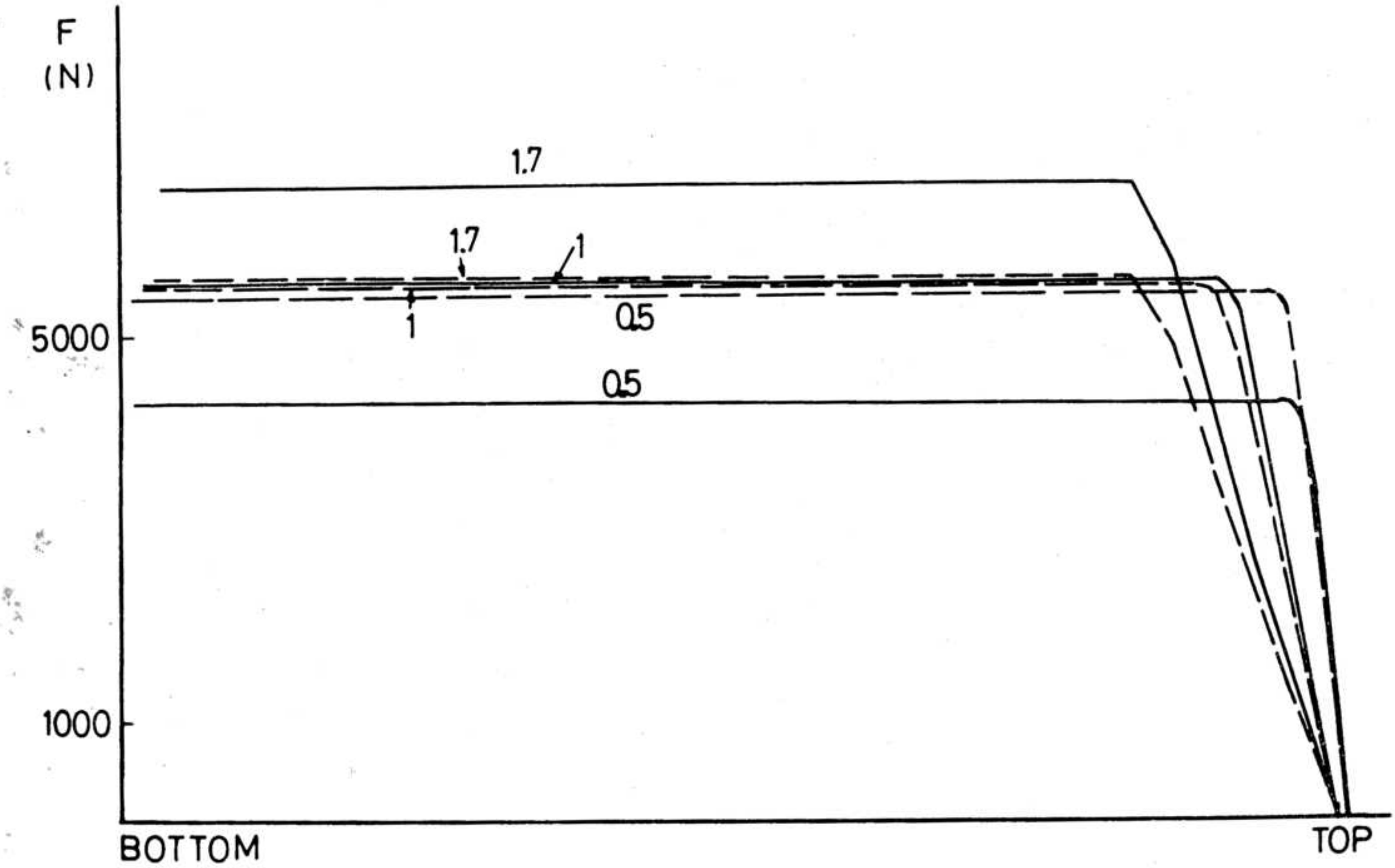

FIG. 9

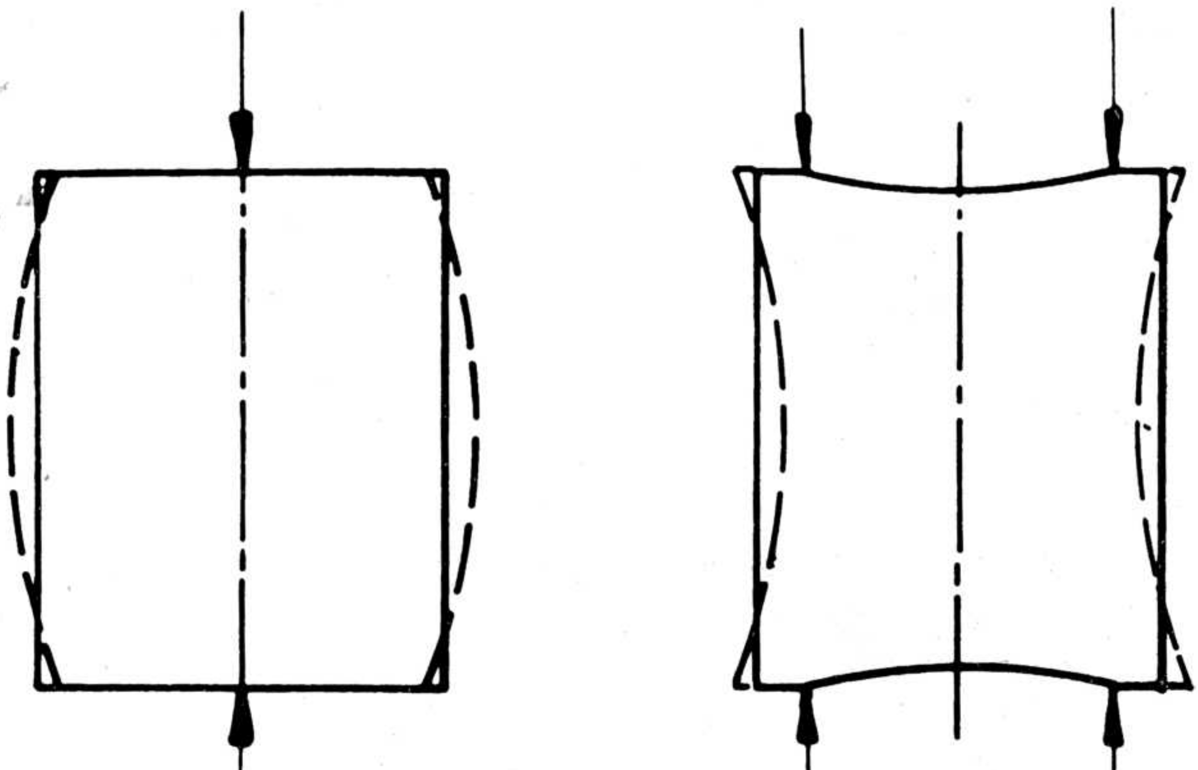

FIG. 10

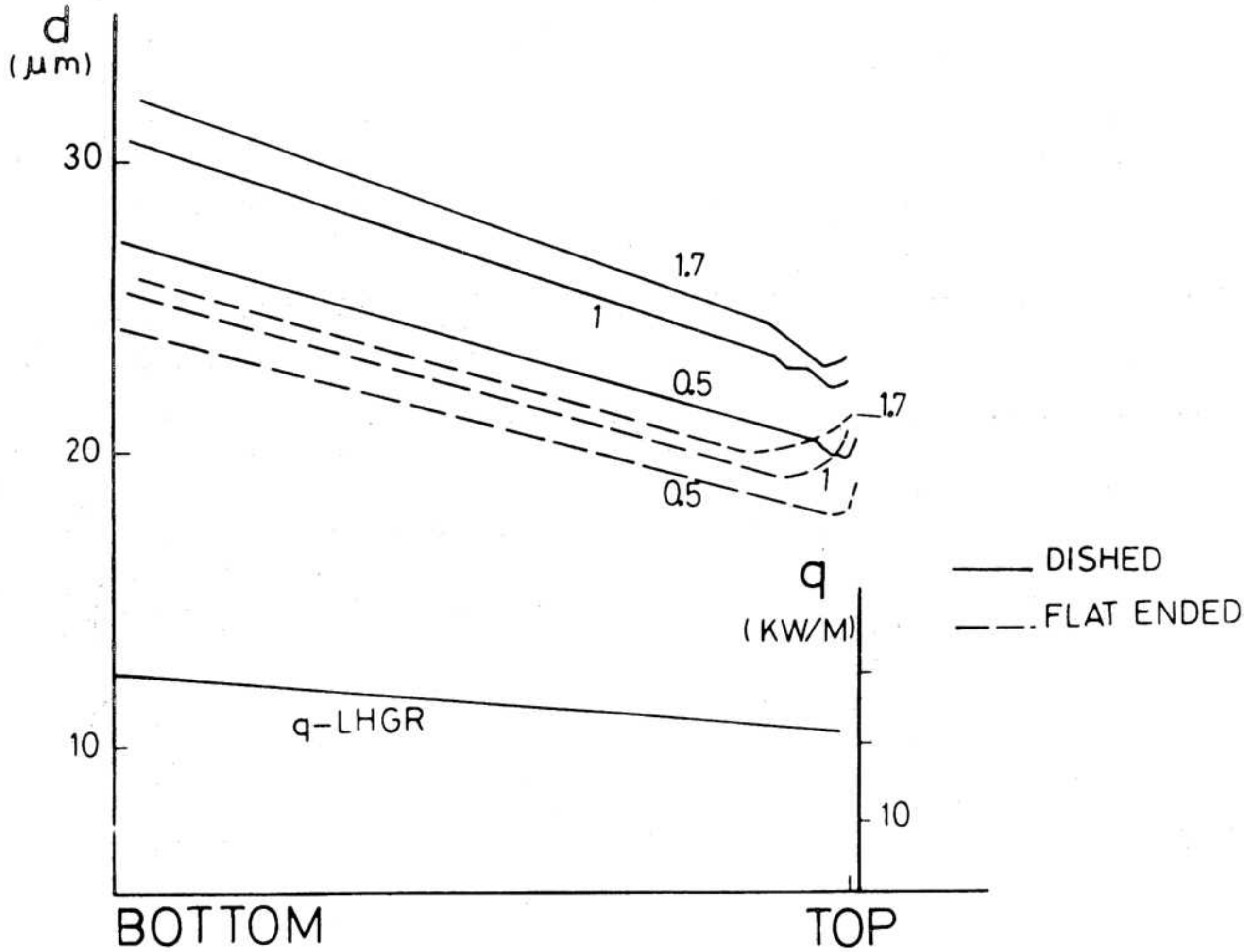
d
(µm)
30
20
10
1.7
1
0.5
1.7
1
0.5
q
(KW/M)
10
DISHED
FLAT ENDED
q–LHGR
BOTTOM
TOP

FIG. 11

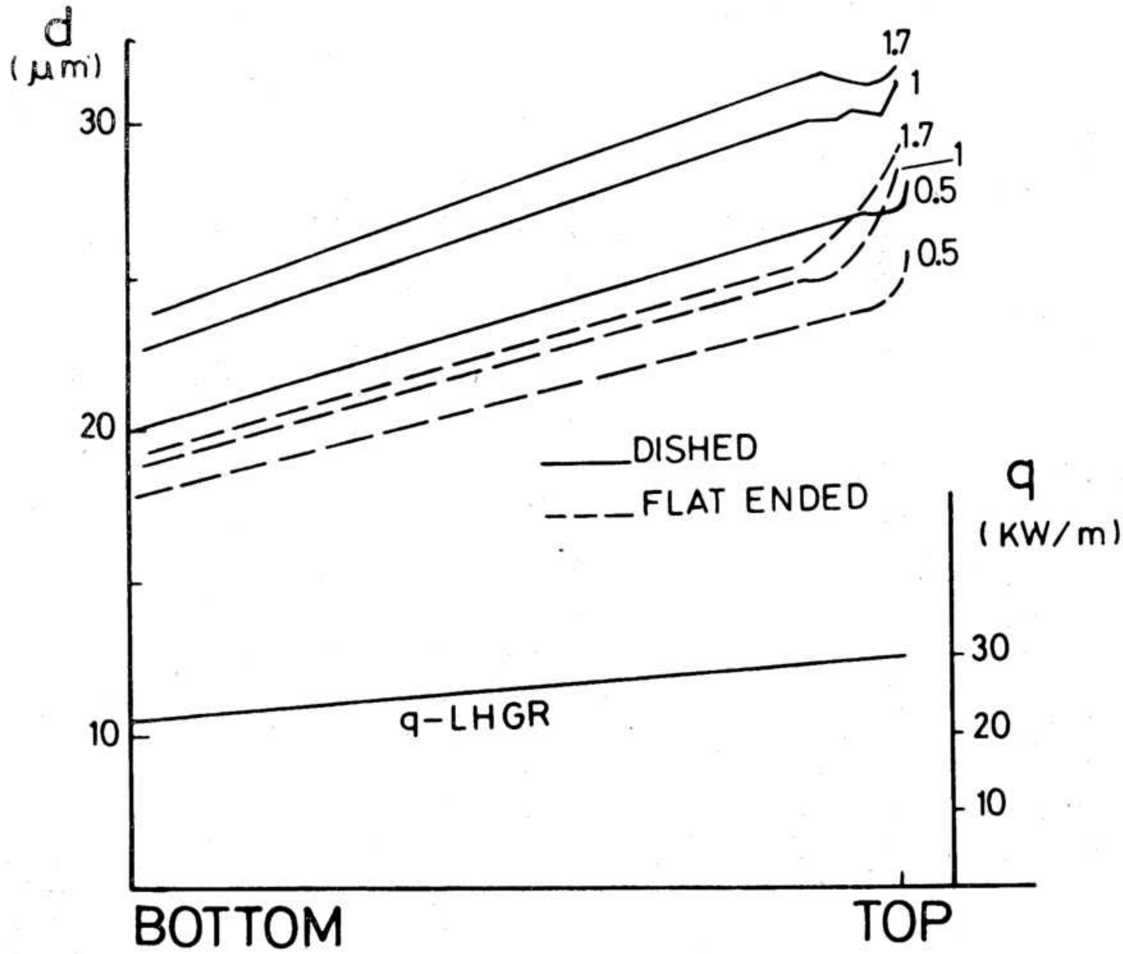
d
(µm)
30
20
10
1.7
1
1.7
1
0.5
0.5
DISHED
FLAT ENDED
q
(KW/m)
30
20
10
q–LHGR
BOTTOM
TOP

FIG. 12

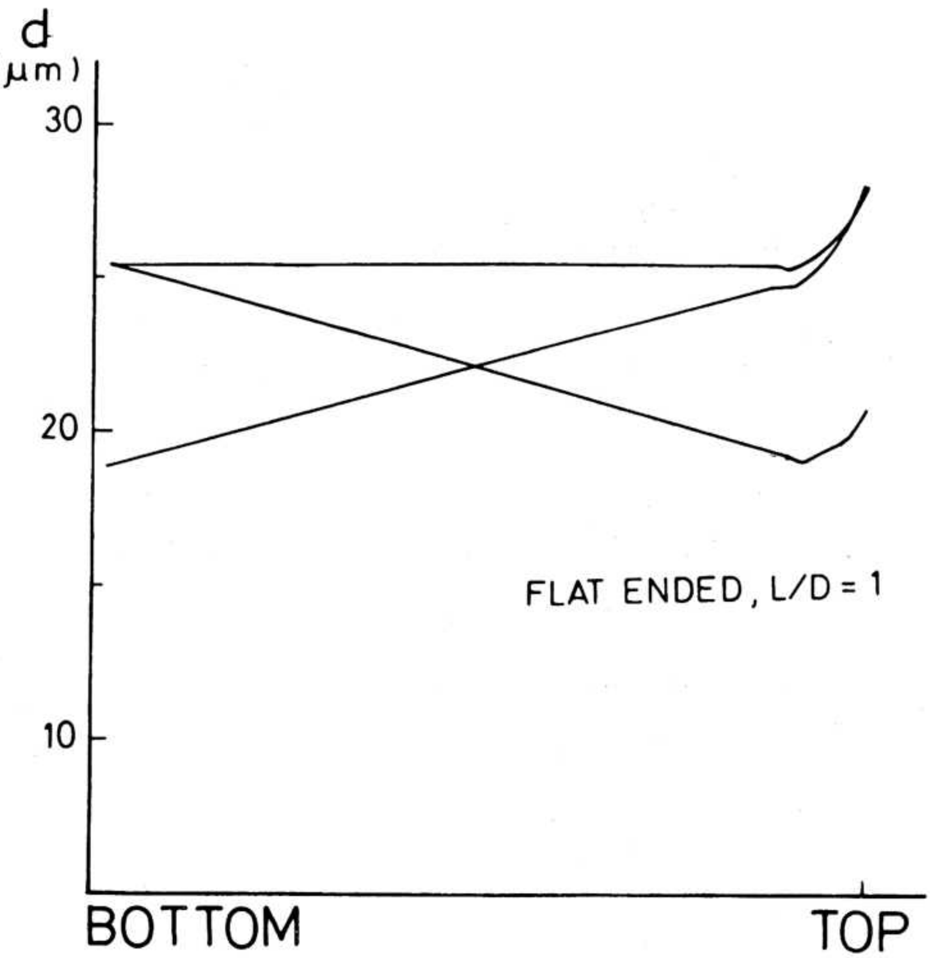
d
(μm)
30
20
10
FLAT ENDED, L/D = 1
BOTTOM
TOP

FIG. 13

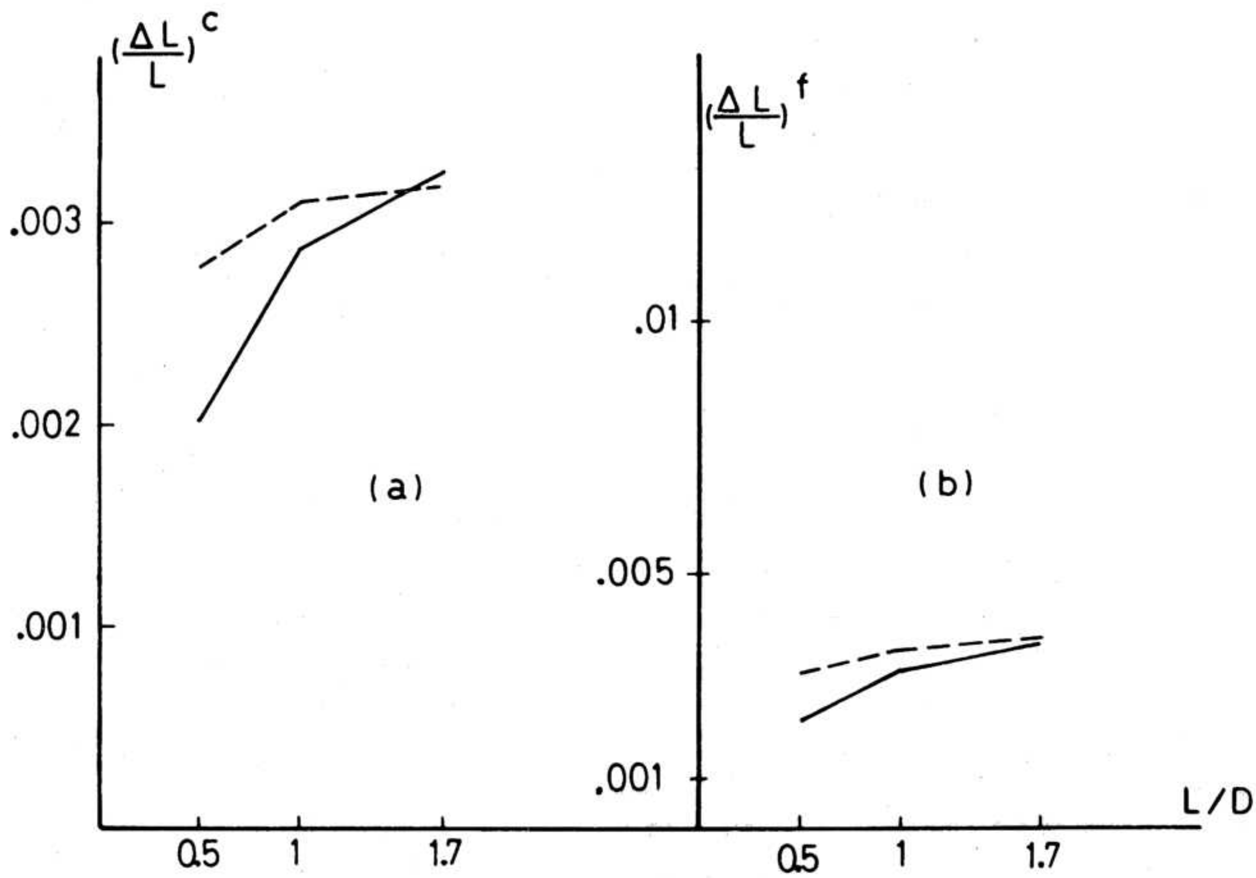
$(\frac{\Delta L}{L})^c$
.003
.002
.001
(a)
0.5
1
1.7
$(\frac{\Delta L}{L})^f$
.01
.005
.001
(b)
L/D
0.5
1
1.7

FIG. 14

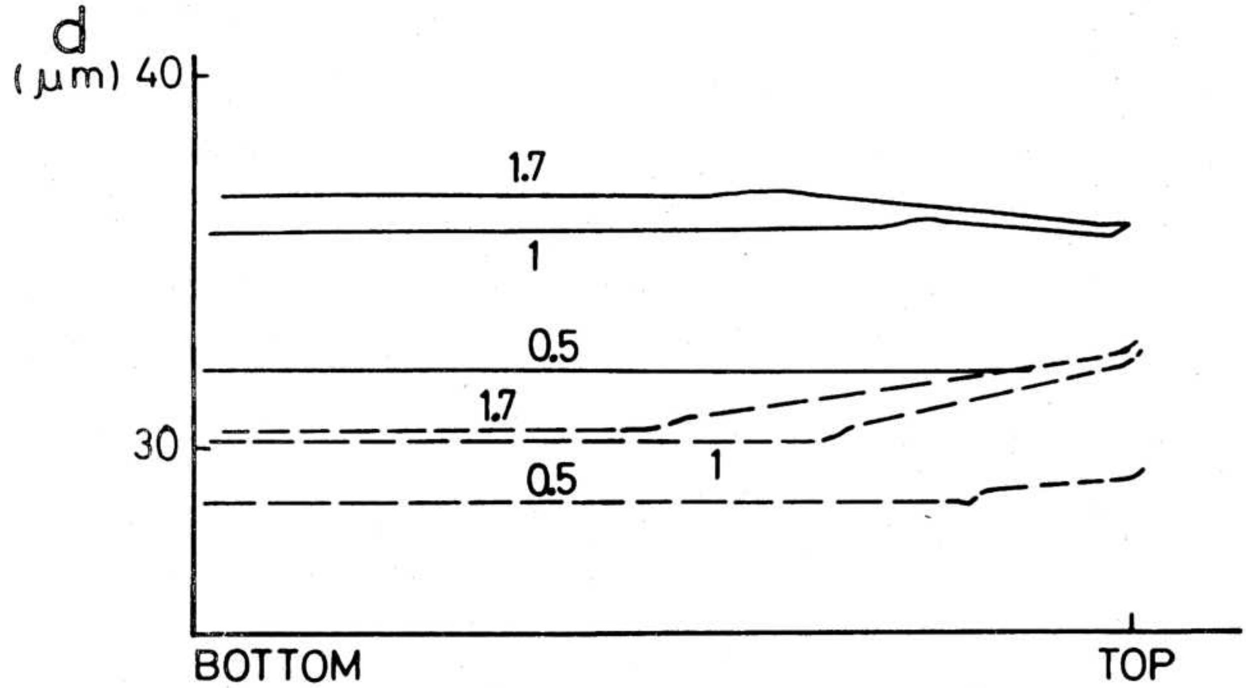
d
(μm) 40
1.7
1
0.5
1.7
30
1
0.5
BOTTOM
TOP

FIG. 15

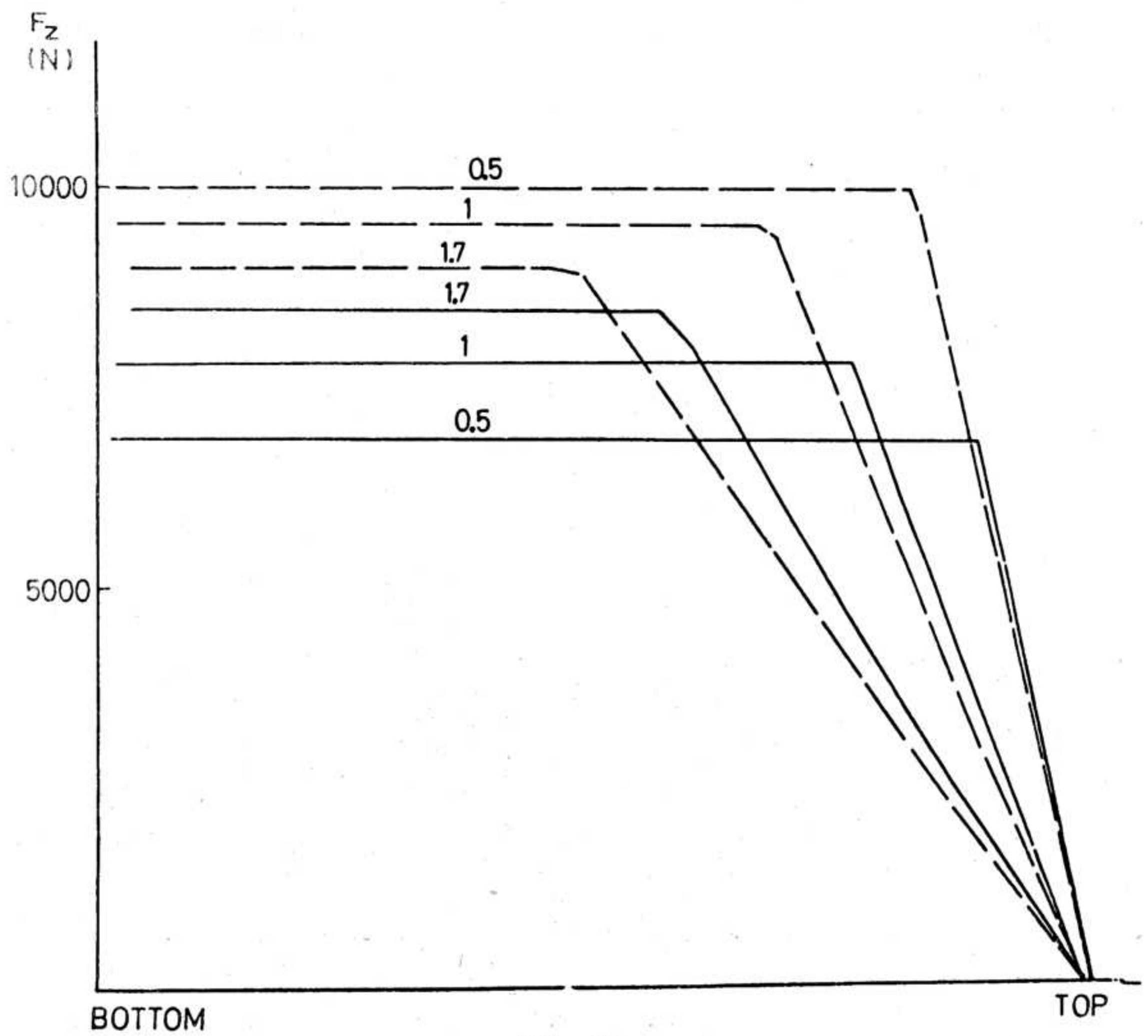
F_z
(N)
10000
0.5
1
1.7
1.7
1
0.5
5000
BOTTOM
TOP

FIG. 16

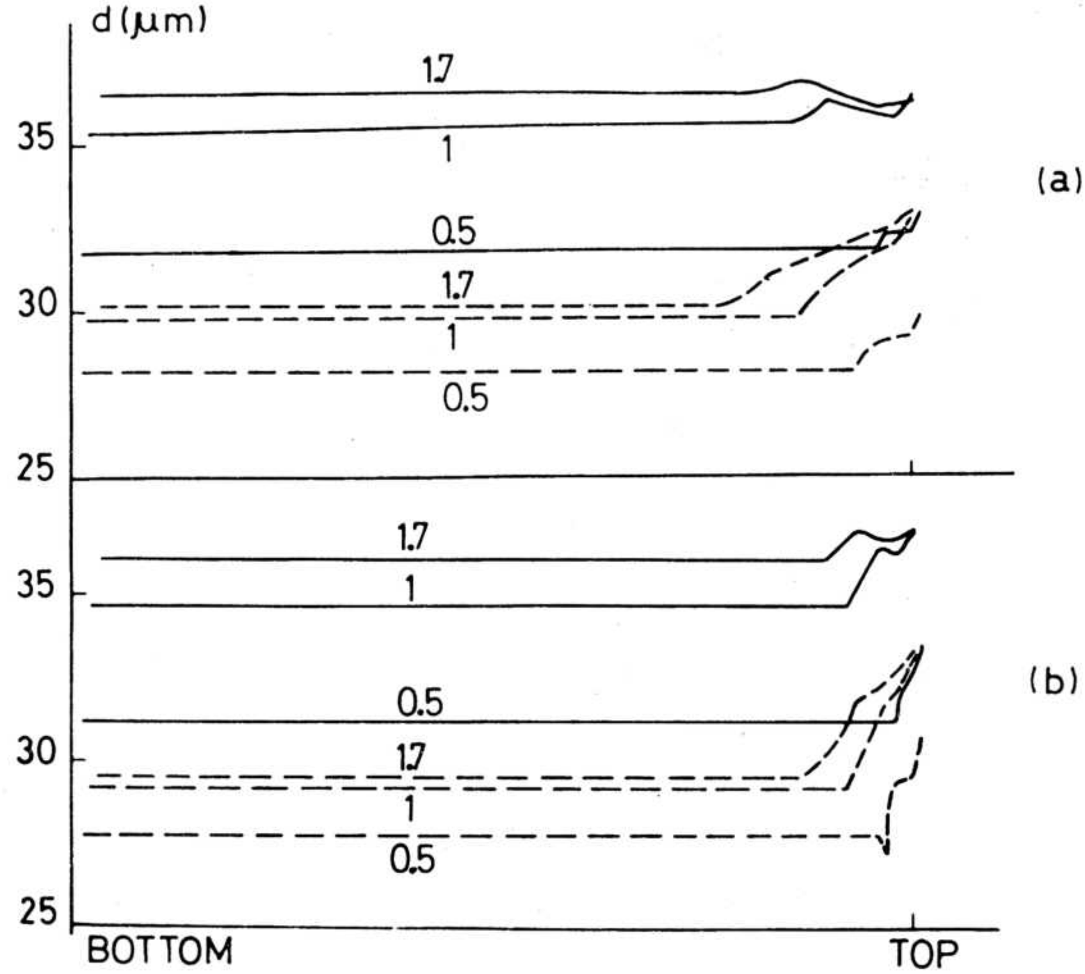
d (μm)
1.7
35
1
(a)
0.5
1.7
30
1
0.5
25
1.7
35
1
0.5
(b)
30
1.7
1
0.5
25
BOTTOM
TOP

FIG. 17

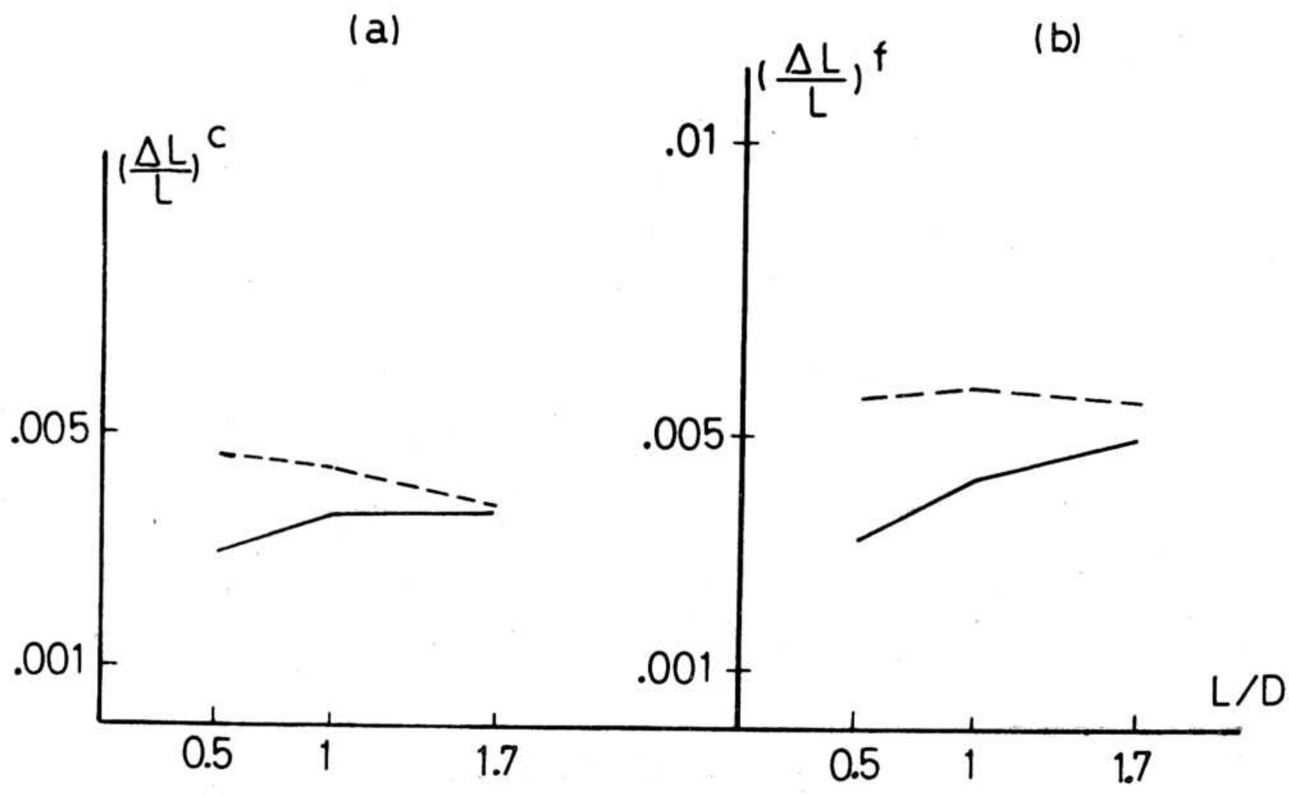
(a)
(b)
$(\frac{\Delta L}{L})^c$
$(\frac{\Delta L}{L})^f$
.01
.005
.005
.001
.001
L/D
0.5
1
1.7
0.5
1
1.7

FIG. 18

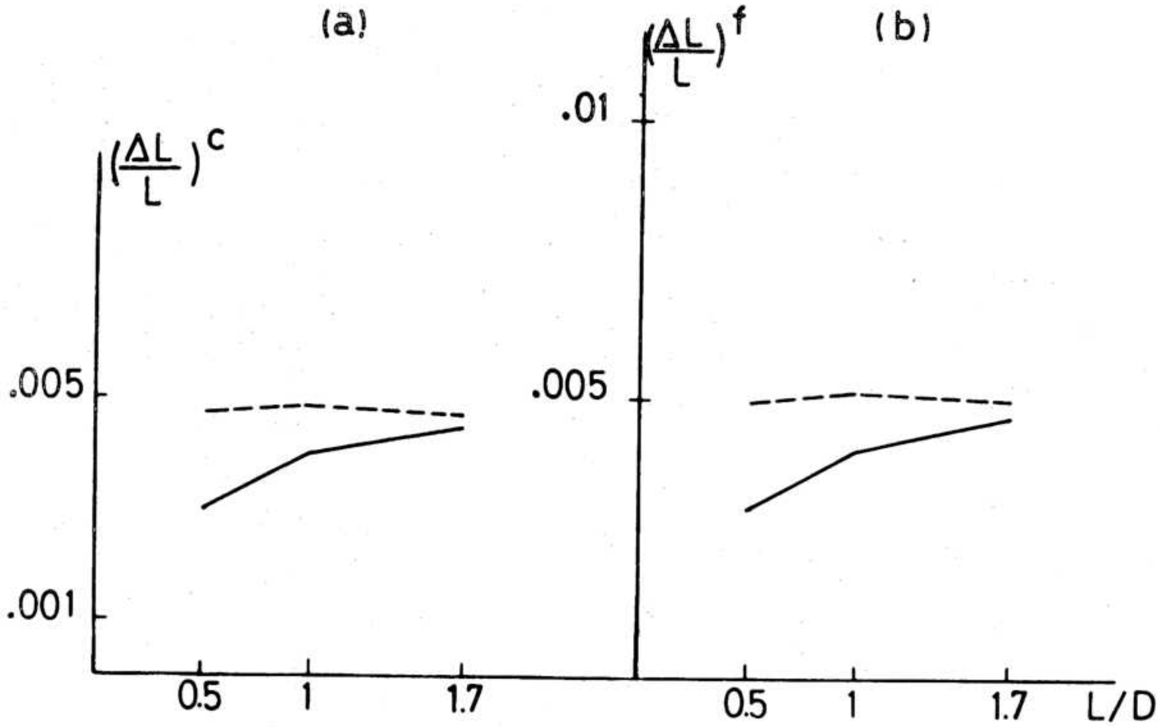
(a)
(b)
$(\frac{\Delta L}{L})^c$
$(\frac{\Delta L}{L})^f$
.01
.005
.001
0.5
1
1.7
L/D

FIG. 19

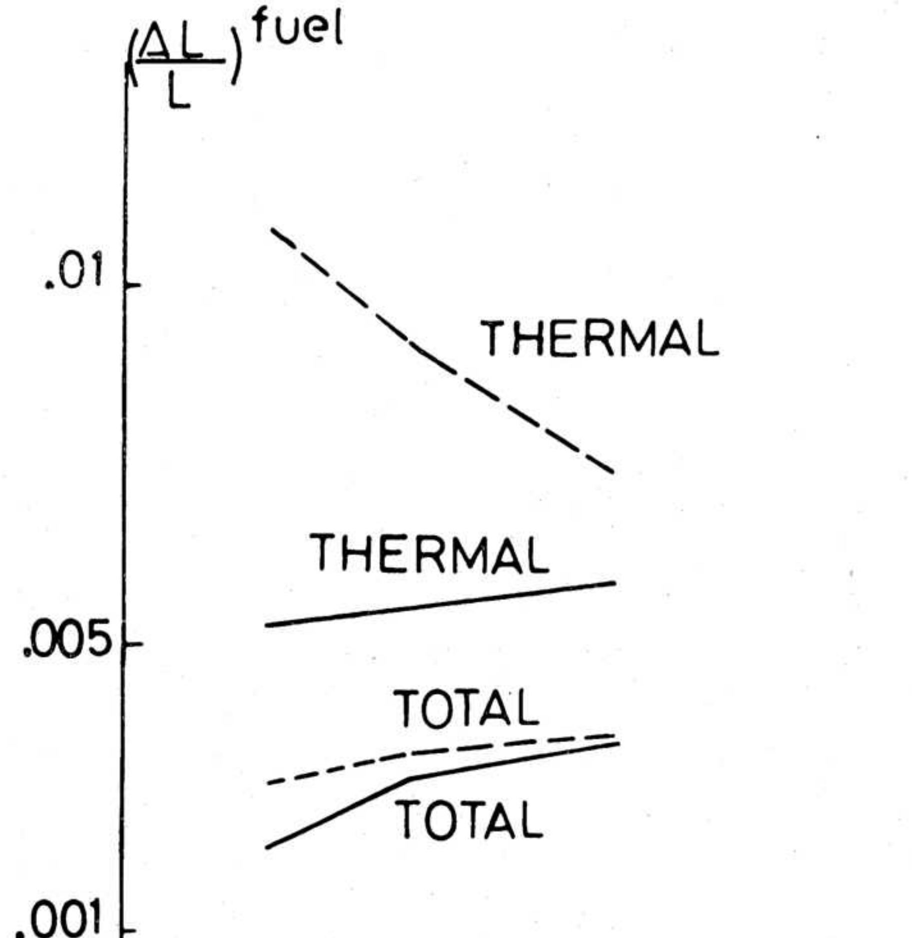
$(\frac{\Delta L}{L})^{fuel}$
.01
.005
.001
THERMAL
THERMAL
TOTAL
TOTAL
0.5
1
1.7
L/D

FIG. 20

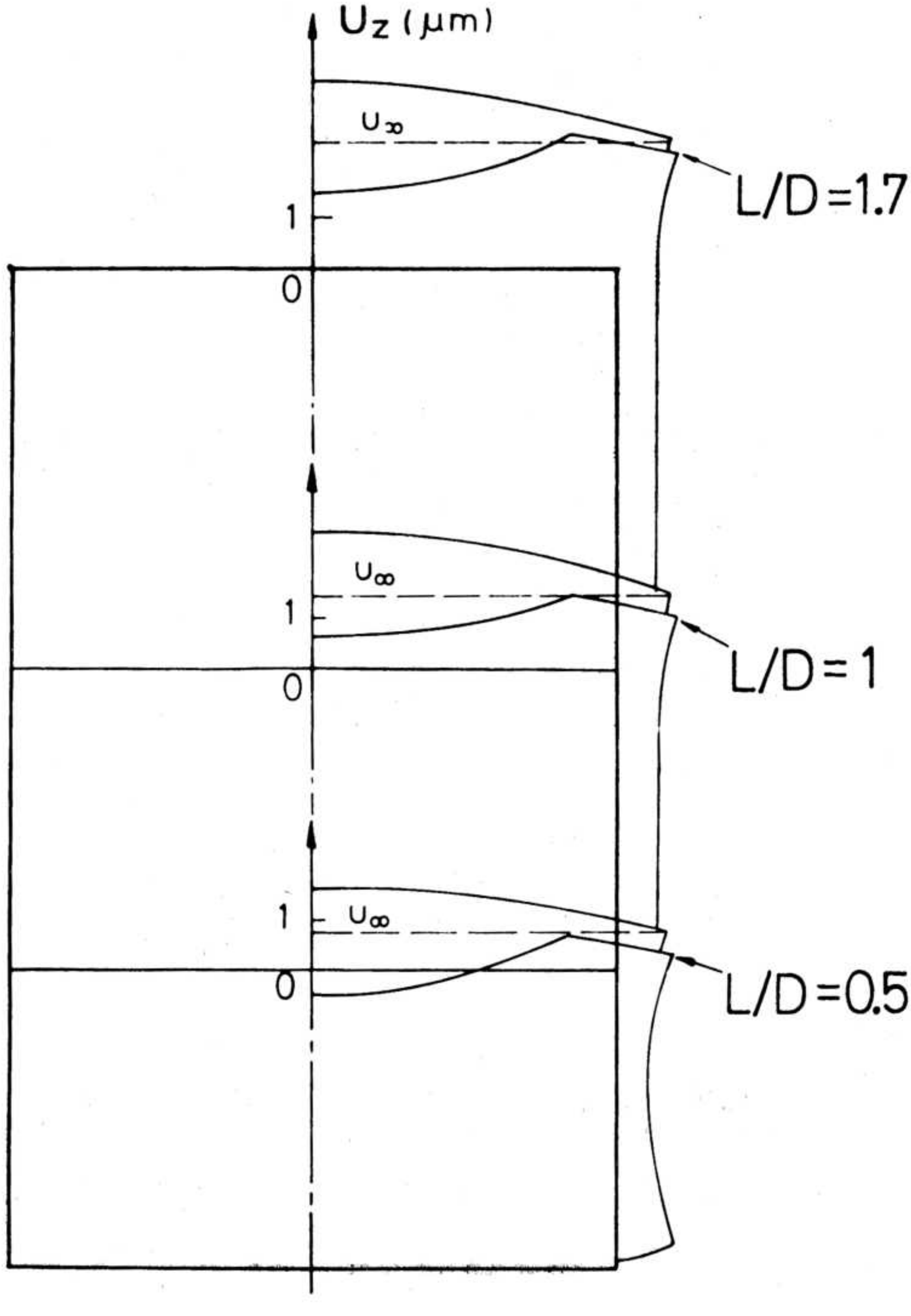

FIG. 21